Aalto University
School of Science

Philip Holm

Neutron detection with high-energy photons using NaI portal monitor

Master´s thesis submitted in partial fulfillment of the requirements for the degree of Master of Science in Technology in the Degree Programme in Engineering Physics and Mathematics.

Espoo, 01.03.2012

Supervisor: Professor Rainer Salomaa

Instructor: Harri Toivonen, Dr. Tech.

Aalto-universitet Högskolan för teknikvetenskaper	SAMMANDRAG AV DIPLOMARBETE
Utfört av: Philip Holm	
Arbetets namn: Neutrondetektering med NaI gammaport genom högenergiska fotoner	
Title in English: Neutron detection with high-energy photons using NaI portal monitor	
Examensprogram: Teknisk fysik och matematik	
Huvudämne: Teknisk fysik	Biämne: Kognitionsvetenskap (vid Helsingfors Universitet)
Professur (kod): Tfy-56	
Övervakare: Prof. Rainer Salomaa	Handledare: Dr. Harri Toivonen (STUK)

Sammandrag:

Nya metoder för neutronmätning utvecklas världen runt på grund av brist på isotopen ^{3}He. I detta diplomarbete beskrivs en indirekt detekteringsmetod som hittills fått mycket lite uppmärksamhet. Metoden utnyttjar högenergiska fotoner som emitteras i neutronreaktioner, så som neutronkapningar och inelastisk spridning. Denna metod har bland annat fördelen att detektorn simultant kan användas som en vanlig gammaspektrometer. Experimentella studier utfördes med en 4”x4”x16” NaI detektor avsedd för portmonitorbruk och ^{252}Cf och AmBe neutronkällor.

Mätresultaten visar att den viktigaste reaktionen är neutronkapning av jod i detektorn. Detektorns effektivitet kan förbättras avsevärt genom att täcka tre av detektorns sidor med polyeten och polyvinylklorid. Plasten fungerar som moderator och konverter. En teoretisk studie över möjliga konvertermaterial begränsade konvertermaterialen till klor och järn. Polyvinylkloriden konstaterades vara en effektivare konverter än järn. Moderatorn och konvertern sänker också backgrundsstrålningen, vilket förbättrar alarmgränsvärdet ytterligare. Konvertern har obetydlig verkan i upp till 4 cm tjocka moderator- och konverterlager. Effektiviteten stiger inte avsevärt med tjockare lager än 10 cm.

NaI detektorn (förbättrad med plasten) jämfördes med en He-portmonitor. Effektiviteten och de minsta möjliga detekterbara aktiviteterna var av samma storleksordning. De facto var dessa värden bättre för NaI detektorn i de flesta fall. NaI detektorn bibehöll sin detekteringseffektivitet bättre då neutronkällorna skyddades med neutronabsorbatorer. NaI detektorn är således ett mycket lovande alternativ speciellt för säkerhetsapplikationer.

Datum: 1.3.2012	Språk: Engelska	Sidoantal: 81
Nyckelord: neutrondetektor, gammaspektrometri, NaI, säkerhetsteknologi		

Aalto University School of Science	ABSTRACT OF THE MASTER'S THESIS
Author: Philip Holm	
Title: Neutron detection with high-energy photons using NaI portal monitor	
Title in Swedish: Neutrondetektering med NaI gammaport genom högenergiska fotoner	
Degree Programme: Degree Programme in Engineering Physics and Mathematics	
Major subject: Engineering physics	Minor subject: Cognitive Science (at the University of Helsinki)
Chair (code): Tfy-56	
Supervisor: Prof. Rainer Salomaa	Instructor: Dr. Harri Toivonen (STUK)

Abstract:

New neutron detection methods are developed worldwide due to the shortage of the isotope ^{3}He. In this thesis, an indirect detection method, that has not received much attention, is described. The method utilizes high-energy photons emitted in neutron reactions such as neutron capture reactions and inelastic scattering. One of the advantages of this method is that the detector can be used as a gamma spectrometer simultaneously. Experimental studies were performed with a 4"x4"x16" NaI portal monitor and ^{252}Cf and AmBe neutron sources.

The measurement results show that the most important reaction is the neutron capture reaction by iodine in the detector. The detection efficiency can be improved significantly by covering three sides of the detector with polyethylene and polyvinylchloride. The plastics serve as a moderator and converter. A theoretical survey of possible converter materials restricted the materials to chlorine and iron. The polyvinylchloride performed better than the iron. The moderator and converter also lower the background radiation, which further improves the limits of detection. The effect of the converter is insignificant if the thickness of the moderator and converter layer is under 4 cm. With thicker layers than 10 cm, the efficiency does not improve significantly.

The NaI detector, boosted with the plastics, was compared with a He portal monitor. The efficiencies and minimum detectable activities were of the same order of magnitude. In fact these values were better for the NaI detector in most cases. The NaI detector preserved its detection ability when neutron shields were used around the sources. The NaI detector is thus a very promising alternative from a security point of view.

Date: 1. 3.2012	Language: English	Number of pages: 81

Keywords: neutron detection, gamma spectrometry, NaI, security technology

Acknowledgements

This thesis was written as part of a research project carried out in the Finnish Radiation and Nuclear Safety Authority (STUK) and funded by the Scientific Advisory Board for Defence (MATINE). I thank both organizations for giving me the opportunity to write this thesis. Especially, I would like to thank the research project leader, my instructor Dr. Harri Toivonen for providing inspirational input on all levels – be it ideas for experiments or scientific writing.

I want to thank my colleagues at STUK, who have helped me with all kinds of problems. I'm grateful for the time Dr. Kari Peräjärvi and Mr Ari-Pekka Sihvonen spent discussing both specific problems related to the thesis and nuclear physics concepts in general. Dr. Arvi Hakanen, Mr Harri Lindroos and Mr Asko Turunen also deserve a special mention. Mr Hakanen and Mr Lindroos assisted me with the measurements and Mr Turunen prepared the efficiency improving booster structures used in the measurements. Last but not least, I'm thankful for the comments on the manuscript by my supervisor, Prof. Rainer Salomaa.

Helsinki, February 23, 2012

Philip Holm

Contents

Symbols and abbreviations

Symbols

Symbol	Description	Page
A	Activity	7
A_a	Active geometrical cross section	25
A_r	Atomic weight	12
A_t	Total geometrical cross section	25
BR_{SF}	Spontaneous fission branching	5
E	Energy	5
F	Neutron production rate	21
I	Intensity or yield	11
I_γ	Gamma ray emission rate	7
k	Boltzmann's constant	11
L_C	Critical level	42
L_D	Detection limit	42
MDA	Minimum detectable activity	42
MDM	Minimum detectable mass	42
N	Atom density	11
n	Neutron	1
P_γ	Gamma ray emission probability	7
r	Distance	25
S	Signal	25
T	Temperature	5
$T_{1/2}$	Half-life	5
t	Time	7
t_L	Livetime	26
Y_c	Isotopical cumulative yield in fission decay	7
Z	Atomic number	5
α	Alpha particle	1
γ	Gamma ray	7
ε	Detection efficiency	25
Θ	Isotopical abundance	15
λ	Decay constant	7
μ	Linear attenuation coefficient	39
$\bar{\nu}$	Mean neutron multiplicity	5
ξ	Average logarithmic energy transfer	12
ρ	Density	39
Σ	Macroscopic cross section	11
σ	Microscopic cross section	11
Φ	Flux	25

Abbreviations

Abbreviation	Description	Page
Bg	Background	26
BPE	Borated polyethylene	23
HPGe	High-purity germanium	20
IAEA	International Atomic Energy Agency	15
LSQ	Least square	28
MATINE	Scientific Advisory Board for Defence	2
MCA	Multichannel analyzer	20
PE	Polyethylene	2
PGAA	Prompt gamma activation analysis	2
PVC	Polyvinyl chloride	2
ROI	Region of interest	27
SF	Spontaneous fission	5
STUK	Finnish Radiation and Nuclear Safety Authority	2

Chapter 1

Introduction

The ^{3}He isotope has provided effective means of neutron detection for several decades. However, the production of ^{3}He has decreased due to the reduced production of nuclear weapons. ^{3}He is a decay product of tritium, which is used in fission and fusion weapons. At the same time, the demand for neutron detectors has increased due to homeland security needs. For these reasons, alternative neutron detection methods are being developed in many research programmes worldwide.

The neutron detection method described in this thesis relies on the detection of high-energy gamma rays (energies higher than 3.5 MeV) emitted either in neutron interactions with matter or directly from a neutron source. The gamma rays can be divided into four categories according to their origin:

- The neutron source itself
- Neutron reactions in the source shield
- Neutron reactions in the environment
- Neutron reactions in the detector system

Only the fourth origin - the detector - can be altered for improvement. This is performed with additional material around the detector („booster") that consists of neutron moderators and converters.

There are four advantages of this indirect detection method. First, the natural high-energy background is very low (good detection capability). Second, high-energy gamma rays can be used to discriminate (α,n) sources from fission sources. Third, light shielding decreases the neutron flux of a source, but massive shielding is required to shield the high-energy gamma rays. This method of neutron detection is thus particularly interesting from a security point of view (evasive scenarios in illicit trafficking). Fourth, the use of normal gamma spectrometers can be extended to neutron detection with very modest adjustments. Only one detector is needed for gamma spectrometry and neutron detection. In fact, the sum is larger than its parts. Normal gamma spectrum analysis can easily be enhanced by the information provided by the high-energy part of the spectrum. Some neutron emitters can be detected by the gamma lines associated with them. However, the identification of the source usually requires very good

energy resolution due to competing gamma lines nearby. In low-resolution spectrometry, the detection of high-energy gamma rays is crucial to have confidence in the correct identification of a neutron emitter.

While investigating an AmBe source in 2008–2009, the Finnish Radiation and Nuclear Safety Authority (STUK) noticed the possibility of detecting neutrons indirectly by detecting the high-energy gamma rays caused by the neutron source [1]. There was already an intention to investigate the subject further in 2010, and some feasibility tests were performed [2]. However, the research project did not start until 2011, when the project was funded by the Scientific Advisory Board for Defence (MATINE).

There is already a planned real-world application of the detection method. The Finnish Customs and STUK are modernizing the border control of radioactive materials with a budget of €10 million. Part of the budget money is being invested in NaI gamma spectrometers. These gamma spectrometers will also be used for neutron detection. Additional security is thus provided with marginal cost.

The approach has been studied by Mitchell et al. (2010–2011) in Refs [3, 4]. In Ref. [3], Mitchell et al. used a 2"x4"x16" NaI detector as a neutron detector by measuring the gamma rays up to 8 MeV. They surrounded the detector with sandwich structures containing polyethylene (PE) as a moderator and either steel or polyvinyl chloride (PVC) as converters. The sandwiches improved the neutron sensitivity of the detector and the improvement was attributed to the high-energy neutron capture gamma rays emitted by the converter materials. The spectra associated with the neutron capture reactions of the converters were calculated in Ref. [3]. However, it is not possible to pin down the reasons for the improvement in sensitivity from the presented measurements alone.

In this thesis, experimental studies on the neutron detection efficiency of a 4"x4"x16" NaI portal monitor and a cylindrical 5"x4" NaI detector were performed. The goal was to understand the underlying phenomena and find an optimum converter. A theoretical survey of potential converter materials was performed using neutron capture gamma data available in a prompt gamma activation analysis (PGAA) database. Iron and chlorine were found to be suitable converter materials and the experimental studies were restricted to these materials. The effect of these converters together with PE moderators on the performance of the detectors was studied. By systematically testing several different converter and moderator structures, insight into the underlying phenomena was gained. The experiments show that neutron capture reactions in the scintillator are of crucial importance. The performance of the NaI portal monitor was compared with that of a ^{3}He tube, using both bare and neutron shielded neutron sources. The NaI portal monitor preserved its detection efficiency better than the ^{3}He tube with the neutron shields.

This thesis is structured as follows: In chapter 2, the characteristic features of fission neutron sources and (α, n) sources are described. Chapter 3 contains the basic theory and concepts of neutron interactions in matter. In chapter 4, the theoretical survey of potential converter materials is described. In chapter 5, the experimental equipment and procedures are described. This chapter also contains the names of the used sources, shields and measurement geometries. The measurement results are presented and discussed in chapter 6. First, the gamma spectra are analyzed and then the performance of the portal monitor is studied. In chapter 7, the performance of the portal monitor with the

recommended converter structure is described. This chapter also contains the comparison with the ^{3}He tube. Chapter 8 contains a summary of the conclusions.

Chapter 2

Neutron sources

Two main types of neutron emission processes are of interest. First, neutrons are emitted in the spontaneous fission (SF) of high Z isotopes, such as ^{240}Pu or ^{252}Cf. Second, neutrons are emitted in alpha capture reactions ((α,n)-reactions) by light nuclei. In certain sources, such as UF_6 or PuO_2, both processes can contribute to the neutron emission [5]. ^{252}Cf and AmBe sources were used in the experiments of this thesis. For this reason, these sources are used as examples in the following description of fission and (α,n)-sources. Some characteristics of plutonium are also included because of the importance of the element in security applications.

2.1 Fission neutron sources

The fission of heavy elements can either be spontaneous with a distinct half-life or induced through neutron capture, for example. The number of neutrons in a nucleus undergoing fission is higher than the sum of the neutrons in the daughter nuclei. The excess neutrons are emitted, carrying part of the energy released in the fission process. The average number of neutrons emitted in a fission event is called the mean neutron multiplicity $\bar{\nu}$.

2.1.1 Neutron yield and spectrum

The spontaneous fission (SF) neutron yield per unit activity of the sample is the product of the neutron multiplicity and the spontaneous fission branching ratio BR_{SF}. Table 2.1 presents $\bar{\nu}$, BR_{SF} and the half-life $T_{1/2}$ of some isotopes of Cf and Pu.

The neutron energy spectrum is approximately a Maxwellian distribution with temperature T [8]

$$\frac{dN}{dE} = \sqrt{E}e^{-E/T}, \tag{2.1}$$

For ^{252}Cf, $T = 1.43$ MeV and for ^{239}Pu, $T = 1.33$ MeV [9]. Figure 2.1 presents plots of equation (2.1) for ^{252}Cf and ^{239}Pu. The energy spectra do not differ much: the difference in the neutron emission of the isotopes is mainly due to the much higher BR_{SF} and shorter $T_{1/2}$ of ^{252}Cf.

Table 2.1: SF neutron yield per activity calculated with the neutron multiplicity and SF branching ratio. Ref. [6] was used except for the values denoted with the superscript „a" (for which Ref. [7] was used)

Isotope	$\bar{\nu}$	BR_{SF}	$T_{1/2}$	SF neutron yield [1/s-Bq]
^{239}Pu	2.32^a	3.1×10^{-6}	24110 y 30	7.19×10^{-6}
^{240}Pu	2.151^a	5.7×10^{-6}	6561 y 7	1.23×10^{-5}
^{250}Cf	3.52^a	0.00077 3	13.08 y 9	0.00271
^{252}Cf	3.7676 47	0.03092	2.645 y 8	0.116

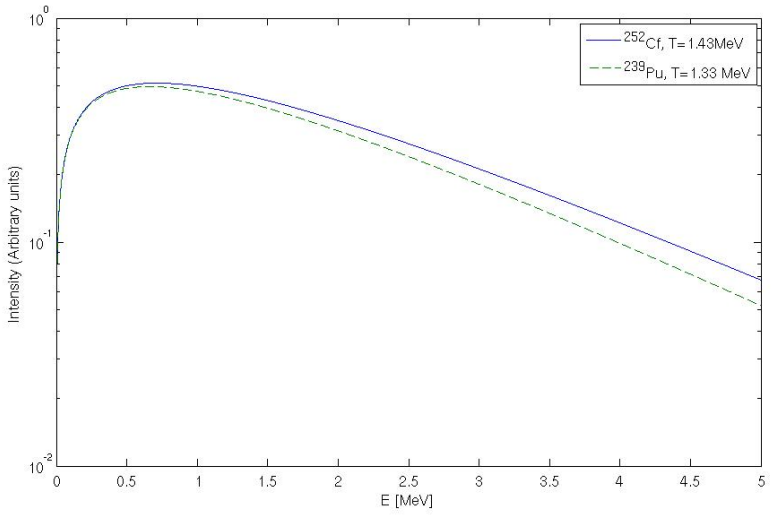

Figure 2.1: Neutron energy spectra for ^{252}Cf and ^{239}Pu according to equation (2.1)

2.1.2 Gamma spectrum

In addition to the neutrons, prompt gamma rays are emitted in the fission event with an isotope-specific photon multiplicity denoting the number of photons emitted in the event. For ^{252}Cf, the average photon multiplicity is about 8 and the average total photon energy is about 7 MeV [10]. The values of other fission sources are similar. Figure 2.2 displays the prompt gamma ray spectrum of the spontaneous fission of ^{252}Cf and the induced fission of ^{235}U+n [11]. The prompt fission gamma rays of ^{252}Cf are distributed as [12]:

$$N(E) = \begin{cases} 38.13(E - 0.085)e^{1.648E} & , 0 \text{ MeV} \leq E \leq 0.3 \text{ MeV} \\ 26.8e^{-2.30E} & , 0.3 \text{ MeV} \leq E \leq 1.0 \text{ MeV} \\ 8.0e^{-1.10E} & , 1 \text{ MeV} \leq E \leq 8.0 \ MeV \end{cases} \tag{2.2}$$

There are also several gamma lines that are associated with other decays than the SF, such as the decay of the daughter nuclide. Due to the different half-lives of the daughter nuclide, it is in some cases possible to determine the age

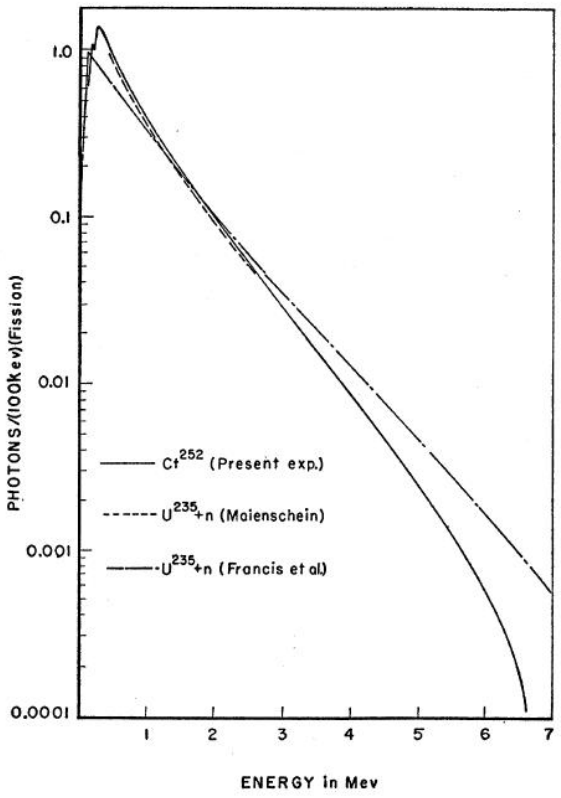

Figure 2.2: Prompt gamma ray spectra of the spontaneous fission of ^{252}Cf and the induced fission of ^{235}U+n [11]

of a fission source by measuring the gamma radiation emitted by the daughter nuclide. The following method is described in Ref. [13], which also contains detailed information on the gamma spectrum of a californium source.

The daughter nuclei ^{137}Cs and ^{132}I can be used for age determination due to their different half-lives (30.1 y and 2.3 h respectively) and close gamma emissions (661 keV and 667 keV). The emission rate I_γ of a gamma ray γ of isotope x at time t is [13]

$$I_\gamma(x) = [\lambda_x/(\lambda_x - \lambda_{Cf})]P_\gamma BR_{SF}Y_{cx}A^0_{Cf}(e^{-\lambda_{Cf}t} - e^{-\lambda_x t}) \qquad (2.3)$$

where λ_{Cf} is the decay constant of ^{252}Cf, $P_\gamma(x)$ is the gamma ray emission probability, Y_{cx} is the cumulative yield for isotope x and A^0_{Cf} is the activity of ^{252}Cf at time $t = 0$. The ratio $I_\gamma(^{137}Cs)/I_\gamma(^{132}I)$ thus only contains known constants and an exponential time function. Because the energies of the gamma rays are so close, differences in the detection efficiency do not have to be taken into account.

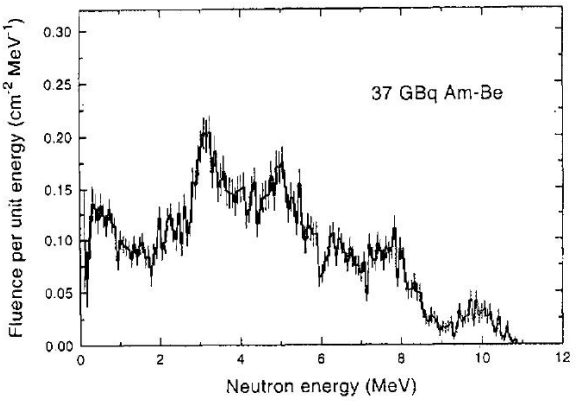

Figure 2.3: Neutron energy spectrum of an AmBe source [14]

2.2 (α,n)-sources

2.2.1 Neutron yield and spectrum

Neutron sources based on (α,n) reactions contain both an isotope that decays by α-decay and an isotope that easily captures the alpha particle and emits a neutron in the process. One example of such a reaction is

$$^{241}\mathrm{Am} \rightarrow ^{237}\mathrm{Np} + \alpha$$

$$^{9}\mathrm{Be} + \alpha \rightarrow ^{12}\mathrm{C} + \mathrm{n},$$

or ^{9}Be(α,n)^{12}C for short. In addition to beryllium, oxygen and fluoride are also important alpha capturers. Uranium and plutonium oxides and fluorides are used in the nuclear fuel cycle.

AmBe sources can be fabricated by mixing the elements or by producing an Am disc and a Be disc, which produce neutrons when in contact with each other. The long half-life of ^{241}Am (432 y) makes it a convenient neutron source. The neutron yield is 70 neutrons/s per 1 MBq alpha activity [8]. Figure 2.3 displays the neutron energy spectrum of an AmBe source. The neutron energy spectrum depends, among other factors, on the energy of the alpha particle[1], the Q-value of the capture reaction and the (α,n) cross sections. The spectrum is also influenced by the macroscopic size of the source [14]. The energy spectrum of, for example, an AmLi (using the reaction ^{7}Li(α,n)^{10}B) is thus very different (the intensity decreases monotonically after a maximum at about 0.1 MeV) [9].

2.2.2 Gamma spectrum

Gamma spectra of AmBe and PuBe sources are presented in Figure 2.4. The line associated with the 4.4 MeV peak and its escape peaks are due to the excited ^{12}C formed in the alpha capture reaction [15]. These high-energy peaks can be used to discriminate between fission neutron sources and AmBe sources.

[1] Note that the alpha particle might loose some energy before being captured

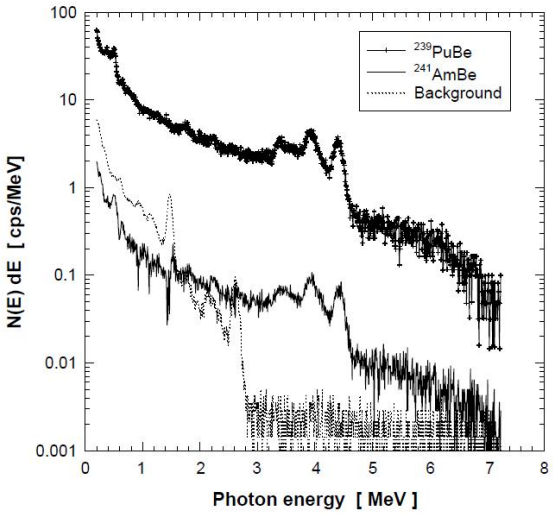

Figure 2.4: Gamma spectrum of a ^{241}AmBe source and a ^{239}PuBe source [15]

Unfortunately, a peak at 4.4 MeV could also be due to a neutron shield containing boron, as is discussed in section 6.2.6. The high-energy gamma radiation of AmBe does in any case provide an effective means of detecting the neutron source.

Chapter 3

Neutron interactions with matter

3.1 Interaction probabilities

The probabilities of different interactions are represented by their respective microscopic cross sections σ. The cross section can be thought of as an effective geometrical cross section encountered by a neutron. The larger the cross section, the higher the probability of the neutron hitting an atom. Generally, the cross sections decrease with higher neutron energies [16]. There are, however, important exceptions, such as resonance regions with large cross sections.

Neutron interactions with matter can be divided into scattering and absorption interactions. Scattering events include both elastic and inelastic events. For low-energy neutrons (E<0.5 eV), elastic scattering and absorption reactions dominate, while for high-energy neutrons (E>0.5 eV), elastic and inelastic scattering processes dominate [8]. When a neutron is in thermal equilibrium with its environment, its average energy is $E_{th} = kT$, where k is Boltzmann's constant and T the temperature of the environment [16]. At 20 °C, E_{th}=0.025 eV. Figure 3.1 presents some neutron cross sections of ^{127}I. Note the large resonance peaks at 0.01–10 keV.

Multiplying the microscopic cross section σ by the atom density N of a sample gives the macroscopic cross section $\Sigma = \sigma N$. This can be used to calculate the fraction of neutrons going through a thin sample of thickness x without any interaction [16]

$$\frac{I(x)}{I_0} = e^{-N\sigma_t x}, \tag{3.1}$$

where I_0 is the incident neutron intensity and $I(x)$ the intensity of neutrons that have not yet interacted. σ_t refers to the total microscopic cross section, i.e. the sum of the cross sections for every interaction.

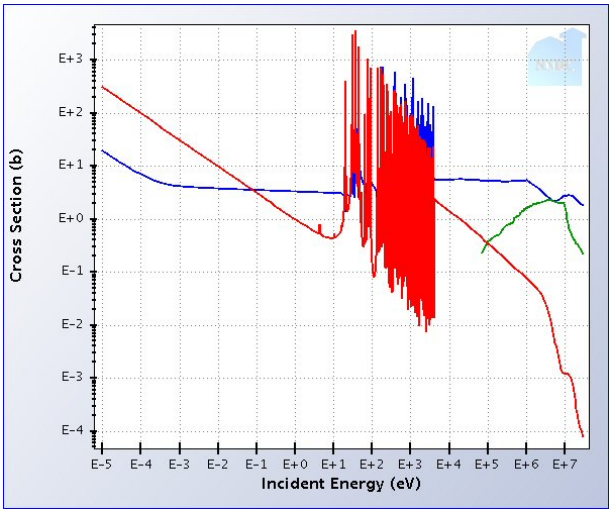

Figure 3.1: The cross sections of ^{127}I for elastic scattering events (red), inelastic scattering events (green) and (n,γ)-reactions (blue) [17]. Note the large resonance peaks.

3.2 Scattering interactions and moderators

In a scattering event the neutron collides with a target atom. Due to the conservation of energy and momentum, part of the energy is transferred to the target atom. This is known as neutron moderation. For an elastic scattering event, the average energy loss ΔE for a neutron with energy E to a target atom with atomic weight A_r is [16]:

$$\Delta E = \frac{2EA_r}{(A_r + 1)^2} \tag{3.2}$$

If the energy of the incident neutron is high enough, the scattering can be inelastic. Part of the neutron's kinetic energy is then used to excite the target atom to an excited state. Because of the larger capture cross sections at lower neutron energies, it is often desirable to moderate the neutrons. Neutrons can be moderated until they are thermal, i.e. in thermal equilibrium with the environment.

Because of the laws of conversion of energy and momentum (see equation (3.2)), light nuclei gain more energy than heavy nuclei in an elastic scattering event and are thus good moderators. Moderators can, however, be compared both by their moderating power and their moderating ratio. The moderating power $\xi\Sigma_s$ is the product of the macroscopic cross section of elastic scattering Σ_s and the average logarithmic energy transfer ξ in the event [16]. By dividing this product by the macroscopic absorption cross section Σ_a we get the moderating ratio $\xi\Sigma_s/\Sigma_a$ [16]. A material with a high moderating ratio should thus be used for moderation, if the absorption of neutrons is undesired. Table 3.1 presents the moderating powers and ratios for a few common moderators [16].

Table 3.1: The moderating power and ratio of common moderators [16]

Moderator	Moderating power (1 eV - 100 keV)	Moderating ratio (approximate)
Water	1.28	58
Heavy water	0.18	21000
Polyethylene	3.26	122
Graphite	0.064	200

3.3 Absorption interactions and converters

The absorption or capture of a neutron by a nucleus can cause the emission of secondary radiation such as protons, alpha particles, photons, one or many neutrons, among others. For high-energy neutrons, the capture cross sections are low compared with the scattering cross sections.

The capture reactions are used for neutron detection. The material (containing e.g. ^{3}He or ^{10}B [16]) that captures the neutrons and emits detectable secondary radiation is known as a converter. The method presented in this thesis relies on radiative neutron capture, i.e. the absorption of a neutron with the succeeding emission of a photon or photons.

Chapter 4

Potential converter materials

For the neutron detector described in this thesis, the converter should be an effective producer of high-energy (>3.5 MeV) gamma rays (or photons)[1]. The gamma rays can either be emitted in inelastic scattering or neutron capture reactions. To understand which elements could be feasible converters, a survey of the high-energy neutron capture gamma rays of different elements was carried out. The gamma rays emitted due to inelastic scattering events are more difficult to take into account, since not only the energies of the excited states have to be considered, but also the probabilities of the decay paths of the state involved.

Neutron capture gamma radiation is utilized in prompt gamma activation analysis (PGAA). PGAA is a non-destructive method to analyze the elemental composition of a sample. The IAEA (International Atomic Energy Agency), among others, maintains an isotopic database with (n,γ) cross sections for thermal neutrons and different photon energies [18]. These cross sections were used to calculate the yield of high-energy photons (from 3.5 MeV to either 8 MeV or 5 MeV) per neutron capture.

The isotopical high-energy photon yield I per neutron capture is

$$I = \frac{\sum_{E_\gamma \geq 3.5MeV} \sigma_{0\gamma}(E_\gamma)}{\sigma_a}, \tag{4.1}$$

where σ_a is the total neutron capture cross section of the isotope and $\sigma_{0\gamma}(E_\gamma)$ is the gamma-ray-specific (n,γ) cross section. σ_a was calculated by summing the (n,γ) cross sections σ_γ obtained from Ref. [18] and the other neutron capture cross sections obtained from the JEF-2.2 database [19].

The elemental yield I^Z can then be calculated by weighting the isotopical yield with the abundances Θ and cross sections

$$I^Z = \frac{\sum_i \Theta_i \sigma_{a,i} I_i}{\sigma_a^Z} \tag{4.2}$$

The yield I^Z together with the cross section gives an idea of what materials could work well as converters. Table 4.1 presents the high-energy photon yields

[1] To some extent low-energy gamma rays can also be useful. They can either add up to form a high-energy peak, or be of such intensity and energy that the peak can be associated with neutron sources.

and the cross sections of different elements. It is, however, important to note that this is not the whole story. Low-energy photon cascades can add up to the high-energy region and the energy efficiency of the detector also influences the detection efficiency.

Out of the elements with reasonably high absorption cross sections, chlorine, iron and cobalt stand out as potential converter materials. Cobalt has both the best photon yield in the 3.5–8 MeV region and the highest absorption cross section. Cobalt powder is relatively cheap, but alloys containing cobalt can be fairly expensive. Cobalt has the additional disadvantage of being activated in a neutron flux. Natural cobalt consists of only ^{59}Co. ^{60}Co has a half-life of ca 5.3 y and decays by β-decay.

Iron and chlorine do not have the same problems as cobalt. ^{35}Cl and ^{56}Fe capture most of the thermal neutrons. The half-life of ^{36}Cl is 301 000 y and ^{57}Fe is stable. Iron and chlorine, which were also used by Mitchell et al. in Ref. [3], were selected as converter materials.

Table 4.1: High-energy photon yields for different elements. The data on the elements marked with the superscript „1" were not complete. The $\sigma_{0\gamma}(E_\gamma)$ values were missing for the following isotopes (Θ in parentheses): ^{11}B (80.1%), ^{106,108,112,114,116}Cd (total 62.49%), ^{112,114}Sn(total 1.63%), ^{144,148}Sm (total 14.31%), ^{156}Gd (20.47%), ^{158}Dy (0.095%), ^{164}Er (1.601%) and ^{208}Pb (52.4%). The yield is assumed to be zero in these cases. The neutron capture cross sections of these isotopes are small compared to the other isotopes of the elements, so the missing data should not influence the results significantly.

Element	Z	σ_a^Z [b]	$I^Z_{3.5-8MeV}$	$I^Z_{3.5-5MeV}$
H	1	0.333	1.8×10^{-7}	0
Li	3	71.5	4.2×10^{-6}	0
Be	4	0.0088	0.79	0
B[1]	5	765	2.6×10^{-5}	1.4×10^{-5}
C	6	0.0035	1.1	1.1
N	7	1.89	0.063	0.017
O	8	0.000279	1.4×10^{-7}	1.4×10^{-7}
Na	11	0.53	0.65	0.40
Al	13	0.231	0.93	0.49
Si	14	0.172	1.5	1.3
Cl	17	33.43	0.7	0.19
Cr	24	3.07	0.23	0.021
Fe	26	3.04	0.79	0.14
Co	27	37.2	0.86	0.18
Ni	28	4.39	0.15	0.035
Cu	29	3.80	0.079	0.079
Br	35	6.4	0.061	0
Rh	45	145	0.053	0
Ag	47	63.3	0.05	0
Cd[1]	48	2522	0.011	0.00034
In	49	272	0.025	0
Sn[1]	50	0.543	0.0015	0.00041
Sb	51	5.13	0.071	0
I	53	6.2	0.16	0.048
La	57	9.08	0.37	0.27
Sm[1]	62	5620	0.0090	0.0037
Eu	63	4560	0.013	0
Gd[1]	64	48800	0.025	0.0088
Dy[1]	66	946	0.056	0.024
Er[1]	68	156	0.10	0.037
Hf	72	119	0.032	0.013
W	74	18.1	0.076	0.036
Ir	77	425	0.072	0.020
Au	79	98.7	0.13	0.014
Pb[1]	82	0.155	0.21	0.00073
Bi	83	0.0338	1.4	1.4

Chapter 5

Experimental

5.1 Moderator and converter measurements

The neutron detection efficiency can be improved by adding moderators and converters to the detector system. This part of the detector is referred to as the booster. Preliminary experiments were performed with a 5"x4" NaI detector and a 1.5"x1.5" $LaBr_3$ detector. Moderating the neutrons with paraffin grains gave promising results (higher neutron detection efficiencies), but converters added to the structures seemed to have little if any effect. In Appendix B, a comparison is made between the performance of the NaI and $LaBr_3$ portable detectors and a portable neutron detector. For the portal monitor measurements, the converter materials were narrowed down to PVC and steel. PE was used as a moderator. Several different structures containing either both moderators and converters or only converters were tested. The focus of this thesis is on the portal monitor measurements.

The moderator and converter measurements were performed in the radiation metrology laboratory in three campaigns (in September 2011 (6 d), October 2011 (4 d) and January 2012 (2 d)). Two Cf sources and two AmBe sources were used. The neutron dose rates of the sources were measured with a Berthold neutron dose rate meter. In principal, the neutron flux can be calculated from the neutron dose rate if the neutron spectrum is known (being e.g. a Cf or AmBe source spectrum). However, because of the large source-detector distance used in the measurements (2 m), the fraction of scattered neutrons was large. The neutron spectrum is thus not known. For this reason, the certified neutron production rates of the neutron sources are used as references for the response of the detectors.

The background radiation was not measured separately in every case. The background has thus not been subtracted from the count rates and efficiencies presented here (except if mentioned). The subtraction of the background from the signal is not a straightforward calculation, since the detectors are activated by the neutron flux. This does not influence the general conclusions, since the signal was large compared to the background. The signal-to-noise ratios presented here are, however, only conservative estimations calculated by subtracting the activated background of the bare detector from the signal and dividing it by the un-activated background of the bare detector.

5.2 Data aquisition

5.2.1 Vasikka

All detectors except the HPGe detector were controlled by the Vasikka software program developed by STUK for in-field measurements. The software acquires spectra and saves them in a LINSSI database[1]. In addition to the administrative data, such as the name of the measurement team, the spectrum together with the measurement time, start and stop time and calibration data are stored in LINSSI.

The standard integration time intervals are 4 s, 40 s and 400 s. The shortest interval (called the search mode), can, however, be set to any value and the other intervals (called monitor 1 and 2) are defined by integer multiplication factors of the search mode time interval. For the portal monitor, the measurement times are 1 s, 10 s and 100 s. Vasikka can handle several detectors simultaneously. For instance, for some of the measurements, the 1.5"x1.5" LaBr detector was connected to a laptop with a USB cable, while the 5"x4" NaI detector was connected to the same laptop using a WiFi connection.

Vasikka has an automatic gain stabilizer that keeps the energy calibration constant. The peak associated with the decay of ^{40}K (emitting a 1460.8 keV photon) was used as a reference for the NaI detectors, whereas the internal contamination related to ^{138}La is used to stabilize the $LaBr_3$ detector.

5.2.2 4"x4"x16" NaI portal monitor

The detector was provided by Environics with a 2048-channel multichannel analyzer (MCA) (Osprey-Canberra Ltd). The gain was set to cover the energy range 0–8.5MeV. The low energy cut off was at channel 5 referring to 14.043 keV. The whole spectrum was recorded along with the sum from channel 863 to 1931 (3499.9 keV - 8003.2 keV). The detector system was operated with the Vasikka software running in the portal monitor mode.

High-energy neutron capture peaks (of iodine and iron) identified in the preliminary measurements and the 4.4-MeV peak emitted by an AmBe source were used for energy calibration. A fourth grade polynomial was used for the fit function[2].

The dimensions of the portal monitor are 140 mm x 140 mm x 1389 mm. The centre of the scintillator is located at 997.6 mm above the ground. For the booster measurements, a 65-cm-high plywood stand was built. The boosters were constructed of PE, PVC and steel plates. The plates on the back side had the dimensions 65 cm x 54 cm and the plates on the detector side 65 cm x 14 cm (covering the side wall of the detector). The thicknesses were 2 cm for the PVC and PE and 3 mm for the steel plates. Different combinations of the plates were tried out. Figure 5.1 shows the portal monitor boosted with a PVC/PE-sandwich. The plywood stand and the booster plates were prepared by Asko Turunen, Provedos Ltd.

[1] See http://linssi.hut.fi/

[2] In the future a piece-wise linear function will be used for energy calibration.

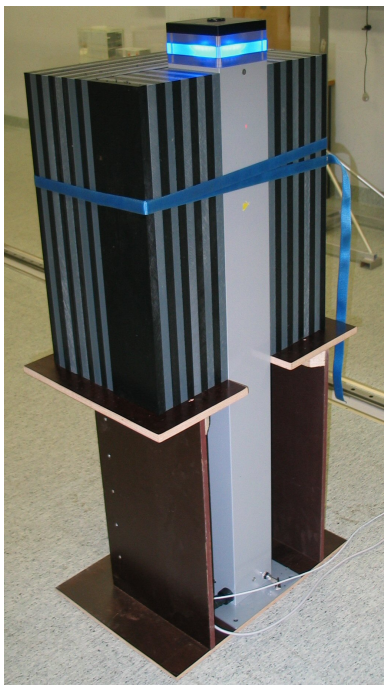

Figure 5.1: Portal monitor boosted with a 20-cm-thick PVC/PE sandwich (the grey plates are PVC and the black plates are PE).

5.2.3 HPGe gamma spectrometer

An Ortec Detective EX HPGe detector was used for some measurements because of its better energy resolution. The dimensions of the HPGe crystal are 50 mm x 30 mm (diameter x thickness, coaxial construction). The MCA has 8912 channels and the energy range was set to 0–11 MeV. The spectra were obtained with MAESTRO software. The docking station of the detector has a small ^{137}Cs source for calibration purposes. The docking station was about 0.5 m from the detector during the measurements.

5.3 Neutron sources and shields

Two Cf and two AmBe sources were available for the measurements. Table 5.1 shows their nominal activities and neutron production rates F according to the manufacturer's certificates. The nominal neutron emission rates during the measurement campaigns are shown in Table 5.2. These emission rates were calculated using the half-lives of ^{252}Cf and ^{241}Am.

All sources were encapsulated with stainless steel. The measurements were performed both with the sources as such (referred to as bare) and with shields around the sources. The shields used are presented in Table 5.3. The plastic shields were used for neutron shielding and the lead shields were used to attenuate the 60 keV peak caused by the americium. The densities of the plastic shields were not known, so the thicknesses were not directly comparable. The

Table 5.1: Activities (A) and neutron production rates (F) of the neutron sources on the reference date of the certificates

Source name	Nuclide	A [Bq]	F [s^{-1}]	Reference date
Cf1	^{252}Cf	4.64×10^7	5.30×10^6	24.6.2002
Cf2	^{252}Cf	4.23×10^8	4.9×10^7	24.10.2000
AmBe1	^{241}Am	1.11×10^{10}	8.41×10^5	3.5.1978
AmBe2	^{241}Am	1.85×10^{11}	1.47×10^7	28.4.1978

Table 5.2: Neutron production rates (F) of the neutron sources at the time of the measurements calculated from the certificate values

Source name	F [s^{-1}](Sep. 2011)	F [s^{-1}](Oct. 2011)	F [s^{-1}](Jan. 2012)
Cf1	4.7×10^5	4.6×10^5	4.4×10^5
Cf2	2.8×10^6	2.8×10^6	2.6×10^6
AmBe1	7.97×10^5	7.97×10^5	7.97×10^5
AmBe2	1.39×10^7	1.39×10^7	1.39×10^7

Table 5.3: Source shields

Shield name	Shield wall thickness and description
SH1	15 cm polyethylene (cylindrical)
SH2	50 cm borated polyethylene (cylindrical)
SH3	31 mm Pb (cylindrical)
SH4	3.8 mm Pb (cylindrical)
SH5	23 cm PE (square)

bare sources were placed on a polystyrene stand at the same level as the centre of the scintillator of the detector, unless otherwise stated. Due to their weight and size, SH2 and SH5 were not lifted from the floor. When these shields were used, the source-floor distance was thus shorter than in the other measurements (45 cm for SH2 and 52 cm for SH5).

5.4 Measurement geometry naming convention

Due to the large number of different measurement geometries, the geometries were named systematically as SOURCE/SHIELD@DISTANCE-BOOSTER, where SOURCE is the source name (see Table 5.1), SHIELD is the shield name (see Table 5.3), DISTANCE is the source-detector distance (from the centre of the source to the surface of the detector). BOOSTER is the name of the booster. Unless otherwise reported, the booster consisted of the booster plates on three sides of the portal monitor (leaving the front side uncovered). If alternating plates of different materials were used, the materials were separated with a slash in the booster name. The material mentioned first was the material closest to the detector. For instance, the PVC/PE-sandwich structure visible in Figure 5.1 was named PVC/PE20cm. More complex structures are described in the text.

For instance, if the 4 MBq Cf source was shielded with 50 cm of borated PE (BPE) and measured at a source-detector distance of 2 m using a 10 cm PVC booster, the geometry was named Cf1/SH2@2m-PVC10cm.

The portal monitor was placed in the middle of the radiation hall in the radiation metrology laboratory. The other detectors were placed on a table ca 1 m from the portal monitor, at the same source-detector distance. Most measurements were performed with the source at a distance of 2 m from the surface of the detector. For other distances, the portal monitor was left in its place while the source and the other detectors were moved.

5.5 Background measurements in different environments

The high-energy background was measured in different environments with the 5"x4" NaI and 1.5"x1.5" $LaBr_3$ detectors. A wooden stand for the detectors was constructed for the measurements. The background was then measured on the roof of the STUK building (both inside and outside), on the ground on an asphalt field near STUK (next to the crossroads of Laippatie and Viilarintie) and at sea. The sea measurements were performed in the Helsinki archipelago around 60°10.675N, 25°10.368E in a sea-alumina ($AlMg_3$) Buster L boat. The water depth was about 16 m and the closest island was at a distance of about 1 km.

Chapter 6

Results

6.1 Calculated quantities

To compare the performance of the detectors, different quantities were calculated from the measurement results. Some difficulties arise, since the gamma spectrometers also detect the gamma rays emitted directly by the source. It is not possible to fully discriminate the pulses caused by the neutrons and the pulses caused by the direct photons. As mentioned earlier, the exact neutron flux was also not known. It is thus impossible to calculate the actual neutron sensitivity of the detectors, and a direct comparison between the gamma spectrometers and conventional neutron detectors is thus difficult to perform.

The absolute neutron efficiency ε_{abs} was chosen as the reference quantity. ε_{abs} is defined as

$$\varepsilon_{abs} = \frac{S}{F} \tag{6.1}$$

where S is the signal of the detector, i.e. the high-energy count rate of the gamma spectrometer, and F is the nominal neutron production rate of the source. As described earlier, the gross count rate was used as the signal S if not otherwise mentioned. In addition to ε_{abs}, the activity response was calculated by dividing the signal by the activity A of the source.

Intrinsic efficiency ε_{int} was calculated using the nominal neutron flux $\Phi = F/(4\pi r^2)$ at the surface of the detector (where r is the source-detector distance). For the calculations, it is possible to use either the active geometrical cross section (the scintillator) of the detector A_a, or the total geometrical cross section A_t (also taking into account the detector cover and the booster). These different efficiencies are referred to here as active intrinsic efficiency $\varepsilon_{int,a}$ and total intrinsic efficiency $\varepsilon_{int,t}$. For the portal monitor, the total cross section was defined as the height of the booster plates (65 cm) multiplied by the width of the front side of the detector system (14–54 cm). The intrinsic efficiencies are thus

$$\varepsilon_{int,a} = \frac{S}{\Phi \times A_a} \tag{6.2}$$

$$\varepsilon_{int,t} = \frac{S}{\Phi \times A_t} \tag{6.3}$$

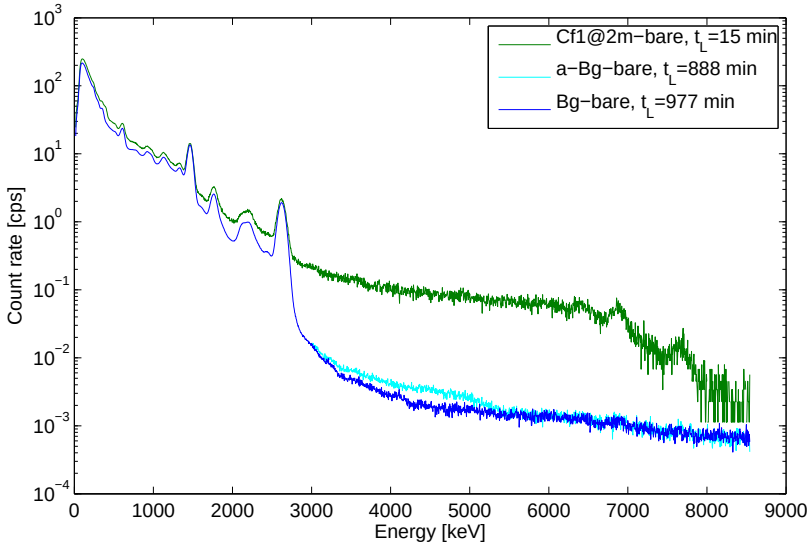

Figure 6.1: Gamma spectra measured with the NaI portal monitor. t_L indicates the livetime. The light blue line shows a background (Bg) measurement performed after the neutron source measurement. The increased count rate up to 5 MeV in the background spectrum indicates that the NaI scintillator was activated by the neutron flux.

6.2 Measured gamma spectra

6.2.1 Gamma spectrometry of a neutron source measured with a NaI detector

Figure 6.1 shows the gamma spectrum of the Cf1 source compared with a background spectrum[1]. The high-energy count rate is much higher with the neutron source present. In the otherwise flat high-energy part of the spectrum, there are peaks at 6.4 MeV, 6.9 MeV and 7.7 MeV. The results are very similar to those presented by Gardner et al. [20]. They activated NaI detectors with neutron pulses and derived the prompt gamma ray spectrum and the decay spectrum.

The 6.4 MeV and 6.9 MeV peaks are identified as neutron capture gamma rays of ^{127}I and ^{23}Na, which are the only naturally occurring isotopes of I and Na. The spectrum can be studied by superimposing the (n,γ) cross sections from Ref. [18]. Such plots are shown in Appendix A. There are relatively high (n,γ) cross sections of ^{23}Na (at 6.4 MeV) and ^{127}I (at 6.7 MeV). The identified

[1]There is an artefact visible in most high-energy spectra presented in this thesis. Some of the channels may contain zero pulses, which cannot be plotted on the logarithmic y-axis. The smallest value shown is thus that of channels with one recorded pulse, visible as a limiting line in the spectra.

reactions are

$$^{127}\mathrm{I} + n \longrightarrow {}^{128}\mathrm{I} + \gamma \xrightarrow[T_{1/2}=25\ \mathrm{min}]{\beta^-} {}^{128}\mathrm{Xe}(93.1\%) \qquad (6.4)$$

$$\qquad\qquad\qquad\qquad\qquad\qquad\qquad\qquad\qquad\qquad \searrow^{EC+\beta^+}$$

$$\qquad\qquad\qquad\qquad\qquad\qquad\qquad\qquad\qquad\qquad {}^{128}\mathrm{Te}(6.9\%)$$

$$^{23}\mathrm{Na} + n \longrightarrow {}^{24}\mathrm{Na} + \gamma \xrightarrow[T_{1/2}=15\ \mathrm{h}]{\beta^-} {}^{24}\mathrm{Mg} \qquad (6.5)$$

Note that sodium has a higher high-energy photon yield per captured neutron than iodine (see Table 4.1). However, the neutron capture cross section of iodine is significantly higher (11.7 times higher for thermal neutrons and 24 times higher for the ^{252}Cf neutron spectrum [17]). The 7.7 MeV peak is due to the stainless steel capsule of the source. There are high (n,γ) cross sections of ^{56}Fe (92% natural abundance) at 7.631 and 7.645 MeV [18] [2]. ^{57}Fe is a stable isotope.

The decay of ^{128}I and ^{24}Na cause an increased count rate up to about 5 MeV, that is visible after the detector has been in a large enough neutron flux[3]. Because of the continuous energy distribution of the emitted β particles, the decay spectra are continuous. Even though the activation of the background spectrum is a small effect, it should be taken into account to minimize false alarm rates. This can be done by having two regions of interest (ROI) in the analysis software: one from 3.5 MeV to 8 MeV (maximum signal) and another from 5 MeV to 8 MeV (free from activation reactions).

The detection efficiency of the β decay in the scintillator is nearly 100%. Assuming that only Na and I contribute significantly to the activated background, the total count rate of the activated detector is

$$\text{total count rate} = A_{0,I}e^{-\lambda_I t} + A_{0,Na}e^{-\lambda_{Na} t} + C \qquad (6.6)$$

where C is the normal background count rate. The constants $A_{0,I}$, $A_{0,Na}$ and C can be fitted to a measured time series of the total count rate. The constants $A_0 = \lambda N_0$ are the activities and N_0 is the number of atoms of the isotopes at $t = 0$. The ratio $N_{0,I}/N_{0,Na}$ is the ratio of the number of neutron captures by I and Na.

To determine this ratio, the 5"x4" NaI detector was activated by putting it close to the Cf2 source for 30 min. The Cf2 source was put inside SH1. The top side of the shield was left uncovered and the detector was put on top of the shield. The background count rate of the detector was then measured without the presence of any neutron source. Equation (6.6) was fitted to the data measured at 1-min intervals (t<3.5 h) or 15-min intervals (t>3.5 h) with 1-min integration times. Due to a technical problem, the measurement stopped

[2] Furthermore, the peak was not visible in the preliminary measurements with the portable detectors. The californium source used in the preliminary measurements had a brass and lead capsule.

[3] The background was 5–30% higher after the measurement campaigns. Since these activations were obtained using the sources in Table 5.1 (Cf1 having a nominal neutron flux of about 9000 $\mathrm{m^{-2}s^{-1}}$ at 2 m), the activation of the scintillator is probably not a major concern in security applications.

at t = 28 h for a period of 12 h. After this, the measurement was continued for 6 hours. Figure 6.2 presents a least square (LSQ) fit of $A_{0,I}$, $A_{0,Na}$ and C to equation (6.6). According to the fit, $N_{0,I}/N_{0,Na} \approx 11.7$. Note that this result is exactly the same as $\sigma_a^I/\sigma_a^{Na} = 6.2/0.53 \approx 11.7$ (see Table 4.1).

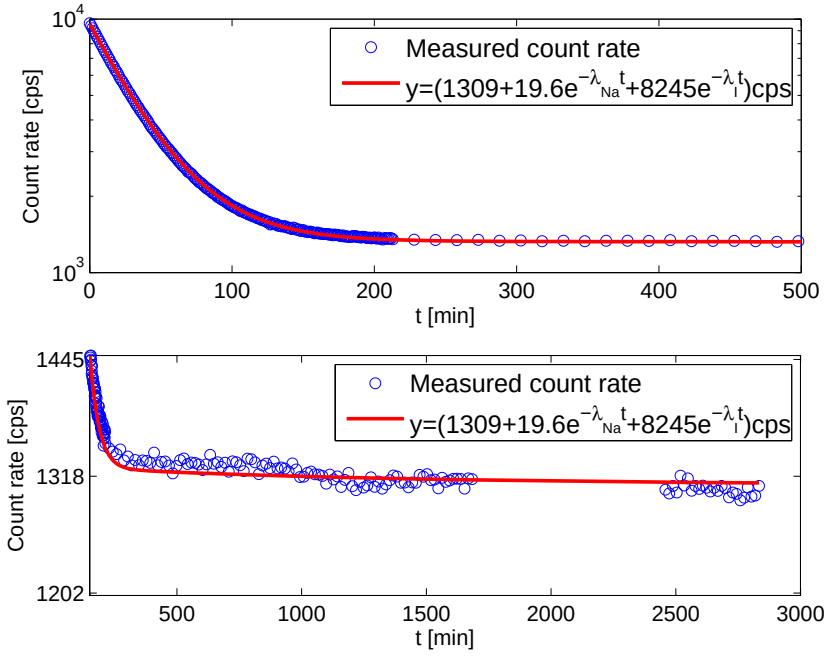

Figure 6.2: Least square fit to the measured decay of the activated 5"x4" NaI detector.

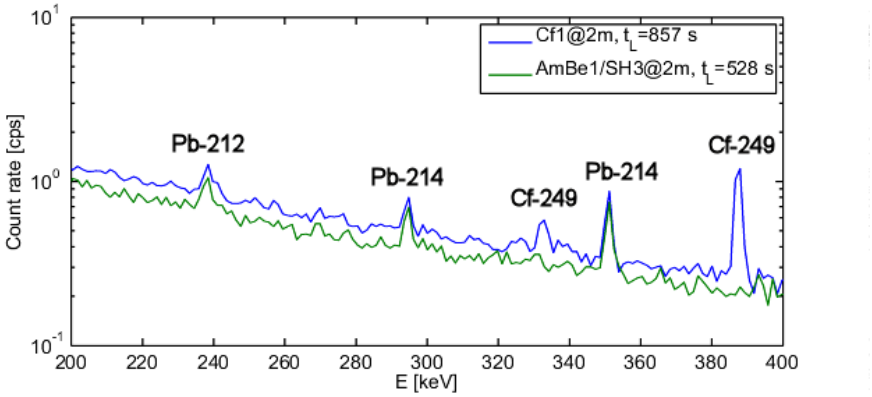

Figure 6.3: Cf and AmBe spectra measured with the HPGe detector. Note the peaks at 333 keV and 388 keV.

6.2.2 Californium gamma spectrum

There are no peaks that are specific to a Cf source in the high-energy part of the spectrum, since the fission photons follow equation (2.2) (see Figure 2.2 for the prompt fission gamma ray spectrum and Figure 6.1 for a Cf spectrum measured with the NaI portal monitor).

The count rate is slightly higher than the background over the whole low-energy part of the spectrum. In addition to this, there is a bump at about 350 keV. With the better energy resolution of the HPGe detector, this bump was resolved into two peaks at 330 keV and 390 keV (see Figure 6.3). These peaks were not visible in the lead shielded AmBe spectra (neither was a bump visible when the bare AmBe source was measured with the portable NaI and $LaBr_3$ detectors). The peaks are most likely due to a ^{249}Cf contaminant in the ^{252}Cf sources. ^{252}Cf sources usually contain significant amounts of other Cf isotopes [21]. This is due to the manufacturing process of the sources. The gamma lines associated with ^{249}Cf are 333 keV and 388 keV. The age of the source Cf1 was 9 y. The half-life of ^{249}Cf is 351 ± 2 y [6], so the relative activity of a ^{249}Cf contaminant grows over time.

For a ^{252}Cf source, there is a possibility of a ^{250}Cf contaminant. As shown in Table 2.1, ^{250}Cf has a SF neutron yield of 2.71 1/s-kBq. Because of the long half-life of ^{250}Cf, the neutron yield of an old Cf source can be larger than expected. Unfortunately, it is difficult to determine the amount of ^{250}Cf due to the lack of detectable gamma rays [13]. This is a significant problem when Cf sources are used for calibration [21]. It is estimated that even 20% of the neutron yield of a 20-year-old Cf source can be due to ^{250}Cf [13]. In this thesis, it is assumed that the Cf sources did not contain ^{250}Cf. The neutron dose rate of the sources used in this thesis have been followed for about 3 years by the staff of the metrology laboratory. The dose rates have decayed by the half-life of ^{252}Cf, but due to the short follow-up time (compared to the half-lives of Cf), no conclusions can be reached. No contaminant abundances are mentioned in the certificate.

In Ref. [13], a method is presented for determining the age of a ^{252}Cf source using the 661 keV peak of ^{137}Cs and the 667 keV peak of ^{132}I (these are fission products of Cf). The measurements performed with the HPGe detector were kept short due to the crystal damage caused by the neutrons. For this reason, it is not possible to properly determine the age of the used Cf sources with these spectra. The following calculations only serve as a demonstration of the method.

The HPGe spectra were analyzed with Aatami[4]. With automated peak search, the software found the ^{137}Cs peak in every Cf source case except when Cf1 was shielded with 50 cm BPE. The ^{132}I peak was only found in the spectrum of the bare Cf2 source. For a better fit, the automatically found peaks were rejected and the nuclide-specific peaks were inserted manually. Figure 6.4 shows the peaks in the Cf2 spectra. The poor data are evident from the figure. In the AmBe spectra, neither peak was found automatically.

The areas of the peak are 238.5 counts (^{137}Cs, uncertainty 12.14% for $k_\alpha = 2.576$) and 49 counts (^{132}I, uncertainty 45.79%). The ratio of the areas is thus 4.87 (uncertainty 47.37%). Using the method described in Ref. [13] (see equa-

[4]Aatami is a radionuclide analysis and evaluation software developed by CTBTO and maintained by STUK

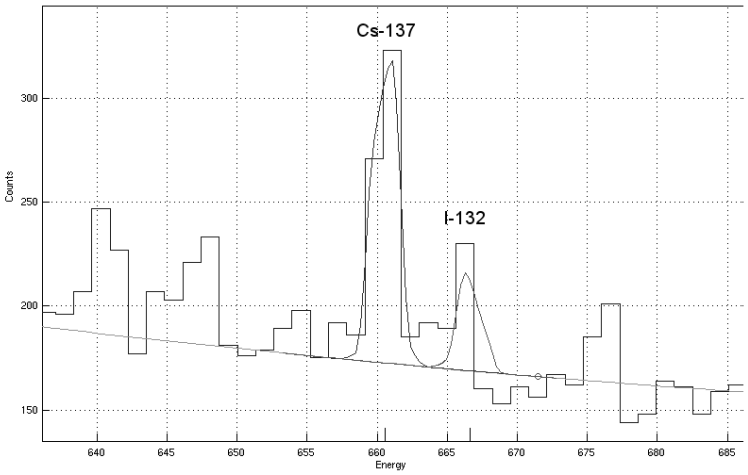

Figure 6.4: Cf2 spectrum measured with the HPGe detector (from 640–685keV). The energy unit is keV and the measurement livetime is 877 s. The gamma peaks of the fission products ^{137}Cs and ^{132}I are fitted to the spectrum.

tion (2.3)), the age was estimated to be 13.8 years. The large uncertainty gives a minimum value of 11.1 y and a maximum value of 15.2 y. Despite the poor measurement data, this fits well with the actual age of source Cf2 (11 years, see Table 5.1).

6.2.3 AmBe spectra

There are two characteristic photon emissions from an AmBe source. First, ^{241}Am emits 59.5 keV photons. The emission rate is so high that lead shields (SH3 or SH4) had to be used to decrease the dead time of the NaI portal monitor. Second, there are the 4.4 MeV photons associated with the excited state of ^{12}C described in section 2.2.2. Figure 6.5 shows an AmBe spectrum measured with the portal monitor.

It was possible to measure the unshielded AmBe source with the 5"x4" portable NaI detector. The measurement showed that shield SH3 caused a 51% decrease in the high-energy signal (see Figure 6.6). Only the 4.4 MeV peak is attenuated, while the lead shield has no effect on the spectrum above 4.4 MeV. The obvious conclusion is that this part of the gamma spectrum is caused by neutron reactions outside the source.

6.2.4 Gamma spectra with steel boosters

Figure 6.7 shows the gamma spectrum of the Cf1 source measured with an 11.5-cm-thick Fe/PE sandwich as a booster (see also Appendix A for spectra with superimposed (n,γ) cross sections). The high-energy count rate is higher compared to the count rate of the PE booster due to the 7.6 MeV neutron capture gamma ray of ^{56}Fe. In addition to the 7.6 MeV and its escape peak, there is also an increased rate at 6 MeV and 7.3 MeV due to neutron capture reactions by ^{56}Fe. The count rate at low energies is lower because of the radiation

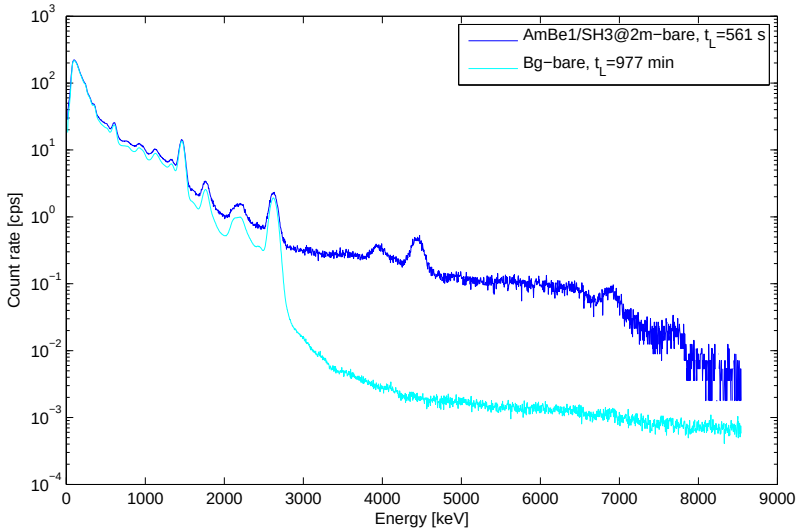

Figure 6.5: AmBe1 shielded with 31 mm Pb and measured with the bare NaI portal monitor at a distance of 2 m

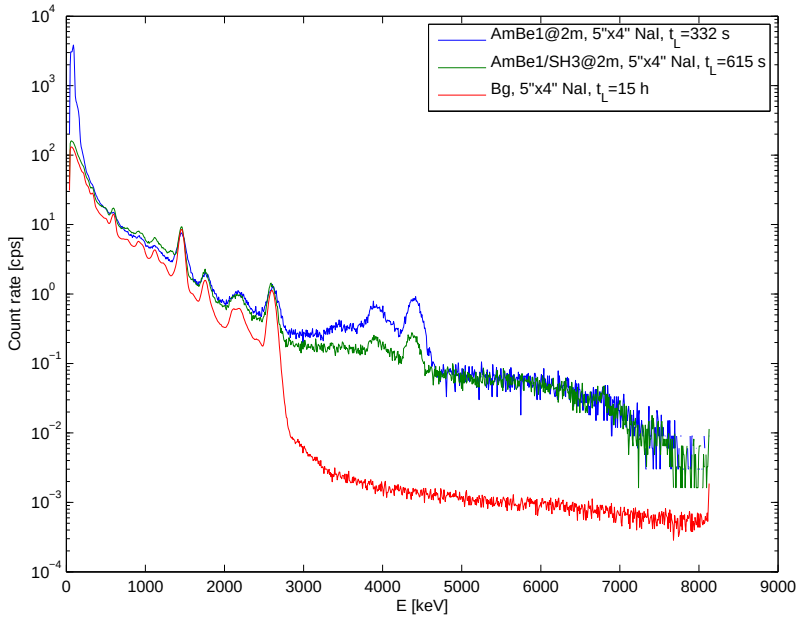

Figure 6.6: AmBe1 measurement with the 5"x4" NaI detector.

shielding of the steel.

With both the PE and the Fe/PE booster there is a peak at 2.2 MeV. This

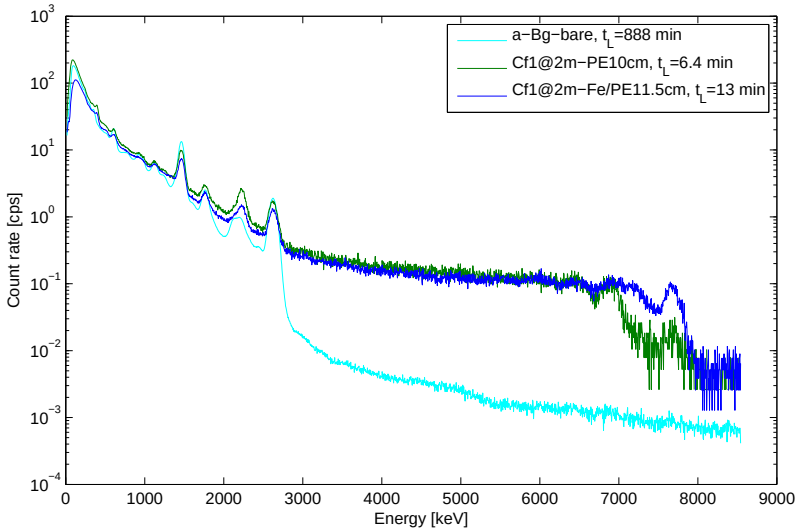

Figure 6.7: Gamma spectra of the Cf1 source with a 10-cm PE booster and an 11.5-cm Fe/PE booster. The background spectrum is an activated background spectrum.

is due to neutron capture by hydrogen in the moderator. With iron present, the peak is smaller, since fewer neutrons are captured by hydrogen (since the iron captures part of the neutrons).

6.2.5 Gamma spectra with PVC boosters

Figure 6.8 displays the gamma spectrum of the Cf1 source measured with the portal monitor boosted with 10 cm of PVC. There are several chlorine-induced peaks visible in the spectrum. There are notable high-energy peaks at 5.6, 6.1, 7.4 and 7.8 MeV, which all seem to be directly related to one or several (n, γ) cross sections of chlorine (see Appendix A). There also seem to be increased count rates due to the (n, γ) reactions producing photons at 517 keV, 2.0 MeV and 2.9 MeV.

6.2.6 Gamma spectra of shielded sources

The source shield measurements were performed in two campaigns. In the first campaign, measurements with the shields SH1 to SH3 (see Table 5.3) were performed. No booster was used. The lead shield (SH3), which had to be used to attenuate the 59.5 keV photons emitted by the AmBe sources, did not fit into the plastic shields (SH2 and SH3). The AmBe measurements were thus not easily comparable.

Shield measurements were also performed in the final comparison between the NaI portal monitor and the ^{3}He based portal monitor (see section 7.3). In this campaign, a 10-cm-thick PVC/PE booster was used. As shown in section 6.3.2, this is a good compromise between performance and size. The shields SH2,

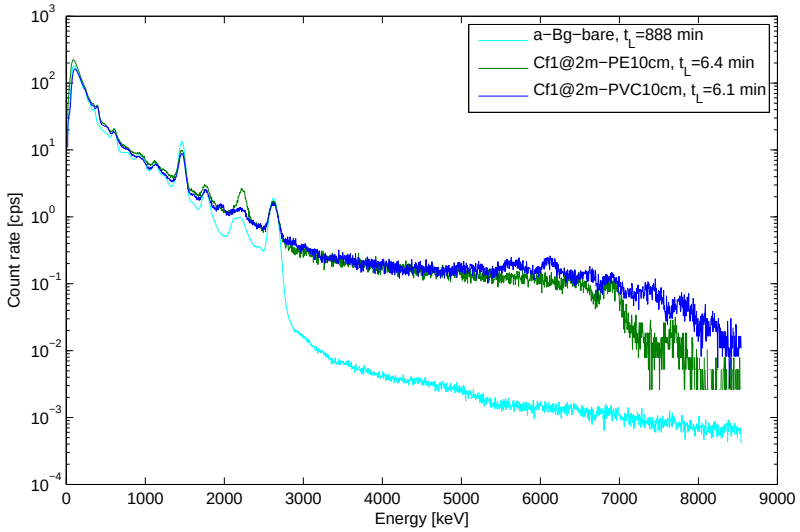

Figure 6.8: Gamma spectra of the Cf1 source with a 10-cm PE booster and 10-cm PVC booster. The background spectrum is an activated background spectrum.

SH4 and SH5 were used in these measurements. The smaller lead shield fitted into the plastic shield and the AmBe measurements were thus comparable. For better comparability, the measurements with the bare source were performed with a source-floor distance of 45 cm[5].

Figure 6.9 displays the gamma spectra of Cf2 with and without SH2. The high-energy count rate is much lower with the neutron shield. The neutron capture peaks of iodine and sodium are smaller, and instead there is a peak at 4.4 MeV. This is due to the ^{11}B in the shield. ^{11}B has an energy state of 4.445 MeV. Therefore the 4.4 MeV peak can be explained by inelastic scattering of neutrons with ^{11}B. The energy of this state is unfortunately very close to that of the excited ^{12}C in AmBe sources. There is thus a risk of identifying a boron-shielded fission source as a Be-based neutron source.

The slope of the high-energy spectrum of the shielded Cf2 source is steeper than that of the bare source. The shielded spectrum has approximately the shape of the fission gamma spectrum (see equation (2.2)). The similarity to the fission gamma spectrum was studied by fitting the measured spectrum to the equation

$$f(E) = Ae^{B\times E} + C \tag{6.7}$$

The LSQ fit resulted in B = 1.0 MeV^{-1} (see Figure 6.10). In equation (2.2), the respective value is 1.1 MeV^{-1}. The spectrum is thus indeed very similar to the fission gamma spectrum, indicating that in the shielded case, a large part of the high-energy signal is due to fission gamma rays.

[5]As described in section 5.3, the source-floor distance was 45 cm with SH2 and 52 cm with SH5

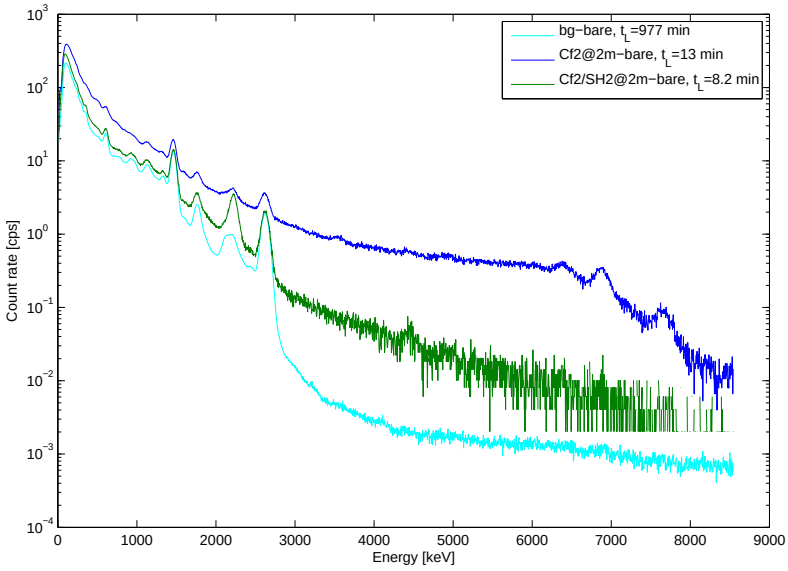

Figure 6.9: Gamma spectra of the bare and shielded Cf2 source measured with the bare portal monitor.

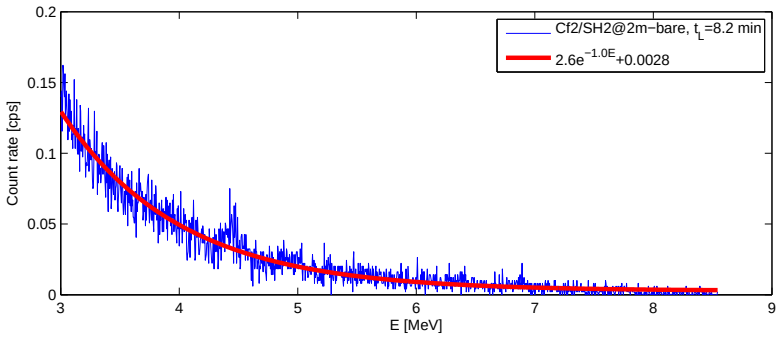

Figure 6.10: The spectrum of the Cf2 source shielded with SH2. The red line represents a fit of equation (6.7) to the spectrum.

6.3 Portal monitor performance

6.3.1 Polyethylene booster

Figure 6.11 shows the absolute neutron detection efficiency ε_{abs} for the Cf1 source at 2 m. The portal monitor was boosted with PE. The booster clearly improves the absolute efficiency, assumingly due to the increased quantity of thermal neutrons in the detector, which increased the number of neutron capture reactions in the NaI scintillator.

There is a maximum efficiency with a PE thickness of 6 cm. After that, the efficiency decreases and saturates. This phenomenon can be explained by

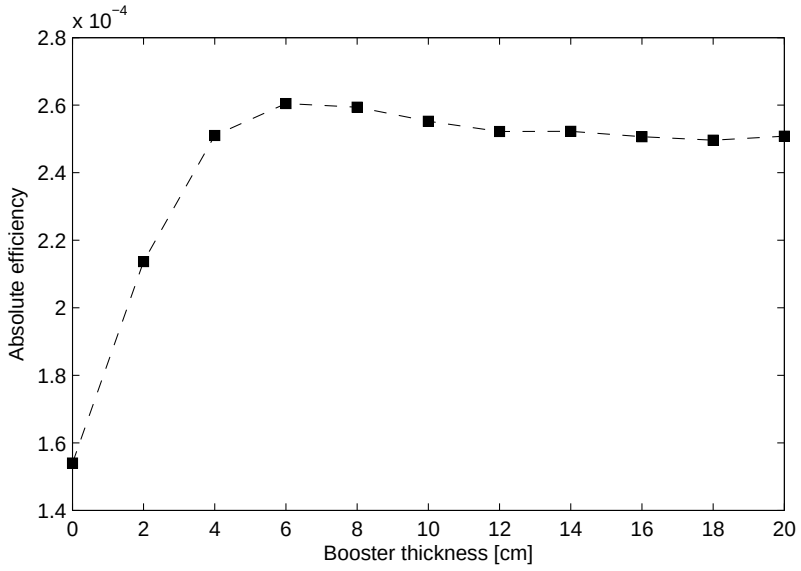

Figure 6.11: Absolute neutron detection efficiency of the portal monitor boosted with PE. The measurement geometry was Cf1@2m-PExcm. The statistical errors of the measurements are small (standard deviation equal to or less than 0.5%.). The gross high-energy count rates were used for the efficiency calculations.

scattered neutrons incident on the side of the detector and absorbed by hydrogen in the PE. Hydrogen only emits a 2.2 MeV neutron capture photon. With a thin moderator, the moderator improves the absolute efficiency to detect the neutrons hitting the detector on both its front side and moderated sides. With a thicker moderator, the absolute efficiency of detecting neutrons hitting the front side of the detector saturates, while the absorption of neutrons decreases the efficiency to detect the neutrons hitting the moderated side of the detector. This causes the curve visible in Figure 6.11. The effect of a moderator on the front side of the detector is discussed in Appendix C. The idea was rejected, since it had only a small or even negative effect on the absolute efficiency (in addition to the fact that it impairs the gamma source detection ability).

6.3.2 Sandwich boosters containing PVC or steel

Figure 6.12 shows the absolute efficiencies of the portal monitor when boosted with simple PVC/PE and Fe/PE sandwich boosters. Alternative booster structures were also tested and are described in Appendix C. Adding the converter material allows the efficiency to be improved beyond the maximum point discussed in the previous section. In fact, the converter thickness seems to have little, if any, effect with booster thicknesses up to 4 cm. This implies that the detector itself is an excellent converter, and the improvement in the absolute efficiency is mostly because of neutron capture reactions in the detector.

Figure 6.12 displays the absolute efficiencies. However, the total intrinsic efficiency $\varepsilon_{int,t}$ rises only using a few centimetres of booster materials, after

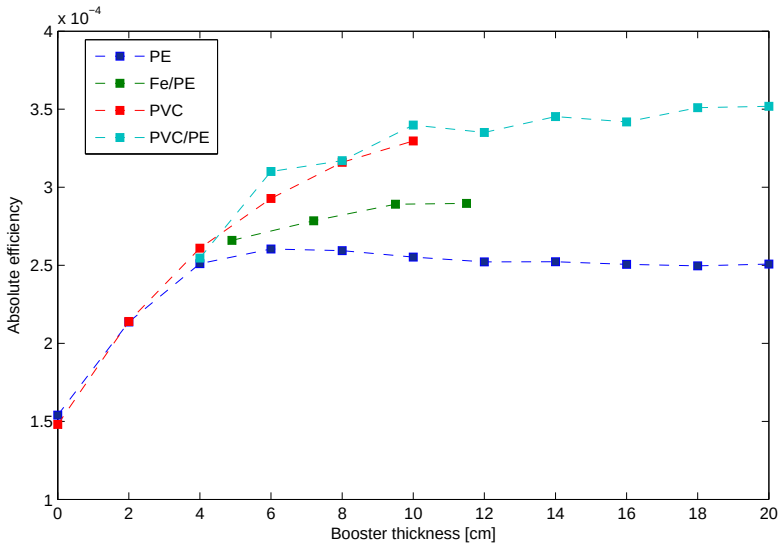

Figure 6.12: Absolute neutron detection efficiency of the portal monitor with different boosters. The measurement geometry was Cf1@2m-booster. The statistical errors of the measurements are small (standard deviation less than 1%). The gross high-energy count rates were used for the calculations. The small difference in the efficiencies of the bare detector (booster thickness 0 cm) shows that the systematic error is negligible.

which it falls drastically. The increased absolute efficiency does not make up for the larger cross section needed. However, the booster materials are cheap and the active intrinsic efficiency $\varepsilon_{int,a}$ naturally has the same booster thickness dependence as the absolute efficiency.

6.4 Source-detector distance dependence

Figure 6.13 shows the absolute detection efficiency of the portal monitor at different source-detector distances. According to the distance law, the absolute detection efficiency should be proportional to r^{-2} (r being the source-detector distance). The efficiency clearly declines slower than this. Fitting power functions to the measurement results shows that the dependence is closer to $r^{-1.1}$ (bare detector) or $r^{-1.5}$ (Fe/PE booster).

The deviation from the distance law is because of the environment, which scatters and moderates the neutrons as well as emitting neutron capture gamma rays. The deviation is larger for the bare portal monitor, since thermal neutrons coming from all sides are detected. With the boosters, a large part of the thermal neutrons scattered from the environment are captured by the hydrogen in the booster.

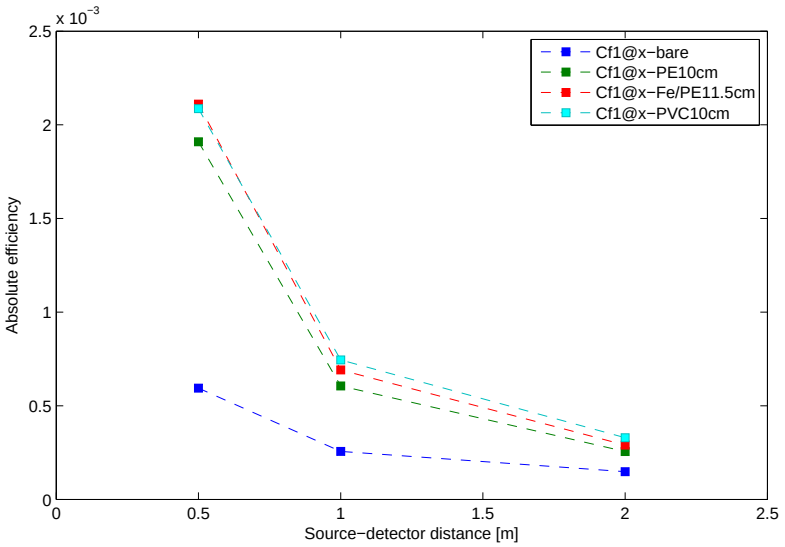

Figure 6.13: Absolute neutron detection efficiency of the portal monitor with different source-detector distances. The statistical errors of the measurements are small (standard deviation less than 1%).

6.5 Background measurements

The order of magnitude of the high-energy background count rate of the portal monitor is only 1 cps. For this reason, background measurements were not performed for every measurement geometry. Another reason for not doing the background measurements was the activation of the NaI scintillator in a neutron flux discussed in section 6.2.1. Instead, the effect of the environment and the booster thickness was studied in separate measurements.

6.5.1 High-energy background in different environments

The measurements in different environments were performed with the boosted 5"x4" NaI detector. Table 6.1 summarizes the results. Some conclusions can be reached from the count rates in Table 6.1. As expected, there is no correlation between the total count rate and the high-energy count rate. The high-energy count rate seems to depend mainly on the amount of shielding from the cosmic radiation. The small laboratory and the radiation metrology laboratory are both on the ground floor of the five-floor STUK building. The high-energy background is clearly higher outdoors. The roof laboratory provides an intermediate value, having only a small amount of shielding.

The high-energy background does not depend on outdoor environment, although at sea the neutron flux seems to be slightly reduced. This should be compared to the neutron backgrounds presented by Kouzes in Ref. [22]. The neutron flux depends on the material interface measured. In Ref. [23], for instance, the reported neutron fluxes at different interfaces are: air/sea 31 n/m^2-s, air/ground 64 n/m^2-s, air/aluminium 210 n/m^2-s and air/iron 770 n/m^2-s. In

Table 6.1: Background count rates of the boosted 5"x4" NaI detector in different environments. The uncertainties refer to one standard deviation.

Environment	Full spectrum [cps] 40 keV - 8.1 MeV	High-energy ROI [cps] 3.5 MeV - 8.1 MeV
Radiation metrology lab.	3480	0.642 ± 0.004
Small lab.	1120	0.644 ± 0.002
Roof lab.	1520	1.027 ± 0.005
Roof	781	1.21 ± 0.02
Asphalt field	1470	1.24 ± 0.03
At sea	40	1.16 ± 0.03

Ref. [24], fluxes of 29 n/m^2-s at an air/water interface and 51 n/m^2-s at an air/ground interface are reported.

The lack of differences in the outdoor high-energy backgrounds could be due to the indirect measurement method. Since high-energy gamma rays can travel large distances in air, not only the measurement interface but the whole environment around the detector is important. The sea aluminium ($AlMg_3$) boat used in the sea measurement could have raised the neutron count rate due to the high neutron background at air/aluminium interfaces compared to air/ground or air/water interfaces. However, the high-energy count rate is actually smaller at sea as compared with the ground measurements.

6.5.2 Effect of a moderator on the high-energy background

Background measurements with PE boosters of different thickness were performed on the second floor of the STUK building. Figure 6.14 shows the background count rates. The PE booster clearly lowers the high-energy background count rate. The high-energy background spectra are lacking the characteristic (n,γ) peaks. This indicates that the origin of the background count rate is mainly in nuclear reactions (e.g. neutron reactions) in the environment. The decrease in the background count rate is thus probably mostly because of the attenuation of high-energy photons from the environment.

The following simple calculation demonstrates that the decrease in the background count rate can indeed be explained by photon attenuation. Figure 6.14 shows that using 20 cm PE, the high-energy count rate decreases to a level of 78% as compared with the bare detector. The fraction of photons passing through an absorber of thickness t is [8]

$$\frac{I}{I_0} = e^{-\mu t} \tag{6.8}$$

where μ is the linear attenuation coefficient. Let us consider 5 MeV photons ($\mu/\rho = 3.045\times10^{-2}$ cm^2/g and density $\rho = 0.9300$g/cm^3 for PE [25]). According to equation (6.8), about 57% of photons do not interact with the material. Correcting this fraction for the fact that one side of the detector is left free gives the fraction 76%, which is almost the same as the measured high-energy count rate decrease.

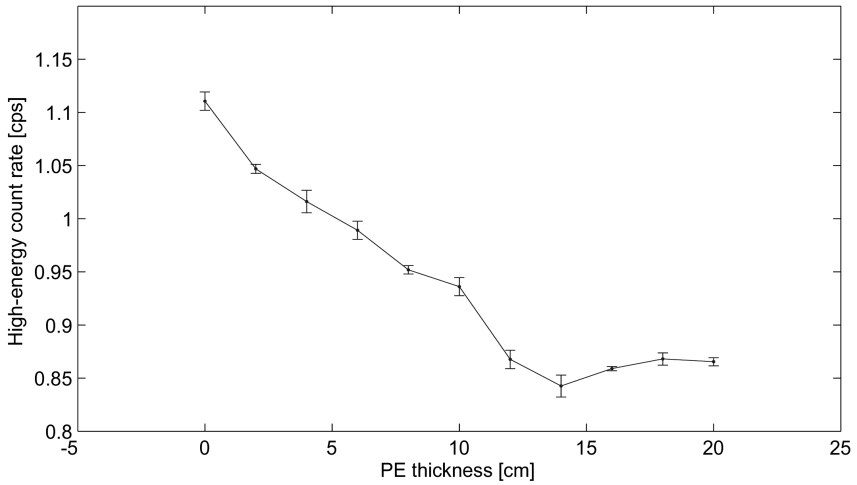

Figure 6.14: High-energy background count rate of the portal monitor with PE boosters of different thickness (leaving the front side bare). The measurements were performed on the second floor of the STUK building. The uncertainties refer to one standard deviation. With a PVC/PE20cm booster, the high-energy background count rate was 0.87, i.e. the same as with the PE20cm booster.

Chapter 7

Performance of the operational portal monitor system

There are some practical restrictions regarding cost, size and weight of an actual portal monitor. The cost of the plastic boosters is not an issue. However, as Figure 6.12 shows, the booster thickness can be restricted to 10 cm without loosing much of the detection efficiency. This reduces the weight and the size of the portal monitor significantly. In this section, the performance of the portal monitor using a 10-cm-thick PVC/PE booster is further examined and compared with the performance of a He-based portal monitor. Note that even though the efficiency of the 10-cm-thick PVC/PE booster is not significantly higher than that of the 10-cm-thick PVC booster, the PVC/PE booster has the advantage of being lighter.

The detection efficiencies and the activity and mass responses are shown in Table 7.1. The measurements were performed with the sources at 2 m horizontal distance from the detector surface and 1 m above the floor. The background was estimated from a short activated background measurement directly after a measurement campaign. The activated background count rate was 1.74 ± 0.07 cps (the un-activated background was 1.639 ± 0.005 cps). Since the activated background changes with time, a higher uncertainty was given to the background count rate: 1.7 ± 0.2 cps. The masses of the sources were not known. However, the mass response for the Cf1 source was calculated assuming a neutron emission rate of 2.30×10^6 n/s-μg for ^{252}Cf [8].

It is important to note that the error margins in Table 7.1 refer only to the statistical uncertainty of the measured counts. A much larger uncertainty lies in the uncertainty of the neutron emission rates and activities of the used sources. The neutron emission rate can vary due to contaminants, such as ^{250}Cf in the Cf source (as discussed earlier). The performance values presented here should thus not be used as calibration values.

Table 7.1: Performance characteristics for source@2m-PVC/PE10cm calculated with the net signal (activated background subtracted). The error margins represent one standard deviation.

Parameter	^{252}Cf (Cf1)	AmBe (AmBe1/SH4)
ε_{abs}	$(3.44 \pm 0.01) \times 10^{-4}$	$(4.68 \pm 0.01) \times 10^{-4}$
$\varepsilon_{int,a}$	0.419 ± 0.002	0.569 ± 0.001
$\varepsilon_{int,t}$	0.0782 ± 0.0003	0.1064 ± 0.0003
Act. response [cps/Bq]	$(3.93 \pm 0.01\times)10^{-5}$	$(3.543 \pm 0.009) \times 10^{-8}$
Mass response [cps/μg]	791 ± 3	-
S/N	92	227

7.1 Limits of neutron detection for the NaI portal monitor

The methods for calculating limits of detection are described in Appendix D. Because of the small high-energy background count rate, exact Poisson solutions have to be used. As described in section 5.2.1, the portal monitor measures spectra continuously with integration times of 1 s, 10 s and 100 s. The 100 s count rate is used as a background measurement. Because of the high data acquisition rate, the false positive alarm rate has to be set to $\alpha \leq 10^{-6}$. The false negative alarm rate is $\beta = 0.05$. Table 7.2 shows the limits of detection in the X@2m-PVC/PE10cm geometry (using sources Cf1 and AmBe1). The background count rate was assumed to be 0.94 cps (see Figure 6.14) and the paired observation case was used (paired observation refers to a not well-known background; background measurement time t_B=100 s). The minimum detectable activities and masses were calculated by dividing the detection limit with the activity (or mass) response).

Table 7.2: Limits of detection for the NaI portal monitor boosted with PVC/PE10cm. t_S indicates the signal measurement time.

Parameter	$t_S = 1$ s	$t_S = 10$ s	$t_S = 100$ s
L_C [cps]	7.06	1.96	0.77
L_D [cps]	14.173	3.05	1.00
MDA (^{252}Cf) [Bq]	$(3.61\ 1)\times10^{5}$	$(7.76\ 3)\times10^{4}$	$(2.55\ 1)\times10^{4}$
MDA (AmBe) [Bq]	$(4.00\ 1)\times10^{8}$	$(8.61\ 2)\times10^{7}$	$(2.822\ 7)\times10^{7}$
MDM (^{252}Cf) [g]	$(1.792\ 5)\times10^{-8}$	$(3.86\ 1)\times10^{-9}$	$(1.264\ 4)\times10^{-9}$

7.2 Source-detector angular dependence

The absolute detection efficiency of the portal monitor boosted with PVC/PE10cm was studied at different source-detector angles. The measurements were performed with the Cf1 and AmBe1 sources at a source-detector distance of 2 m. In this series of measurements, the source-detector distance was measured from the centre of the detector system including the booster (instead of the detector surface). Figure 7.1 displays the normalized efficiencies for the Cf1 and AmBe1 source, respectively.

The absolute detection efficiency is essentially the same at 0° and 30°. With larger angles, the efficiency decreases, since the booster gets in between the source and the detector. The minimum efficiency at 120° coincides with the maximum booster thickness. The efficiency at this angle might improve with the (intended) rectangular shape of the portal monitor. Another factor contributing to the angular dependence of the detection efficiency is the geometrical cross section of the portal monitor, as seen from the source. This lowers the efficiency when the source is on the side of the detector (at 90°).

The angular dependence of the absolute efficiency is similar for the Cf1 and the AmBe source. The angular dependence is, however, more uniform for the Cf1 source than for the AmBe1 source. For instance, at 180°, the efficiencies are 78% (Cf1) and of 73% (AmBe1) of the respective maximum efficiencies.

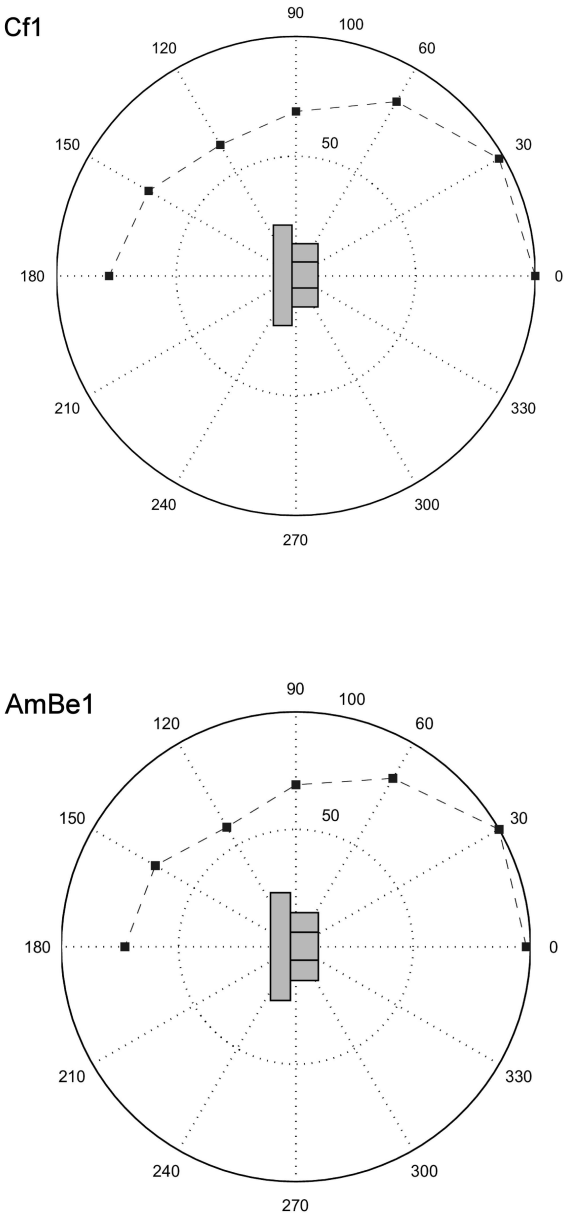

Figure 7.1: Angular dependence of the detection efficiency in the X@2m-PVCPE10cm geometry. The efficiencies have been normalized to the maximum value of the respective source. A horizontal cross section of the boosted detector is shown in the graphs. The statistical errors of the measurements are small (standard deviation less than 1%).

7.3 Comparison with standard neutron portal monitor based on ^{3}He

The performance of the NaI portal monitor was compared with a portal monitor based on ^{3}He. The He-based portal monitor consisted of a Thermo Fisher Scientific ^{3}He tube with the dimensions of 4.9 cm x 81.3 cm (active diameter x length). The active cross section area of the ^{3}He tube was thus only slightly smaller than that of the NaI portal monitor (399 cm^2 compared to 413 cm^2). The ^{3}He tube was inside a plastic tube with diameter of 16 cm filled with PE grains. The high voltage was 1500 V (the same as in normal use). The count rate and its uncertainty were estimated from a moving 30-s average.

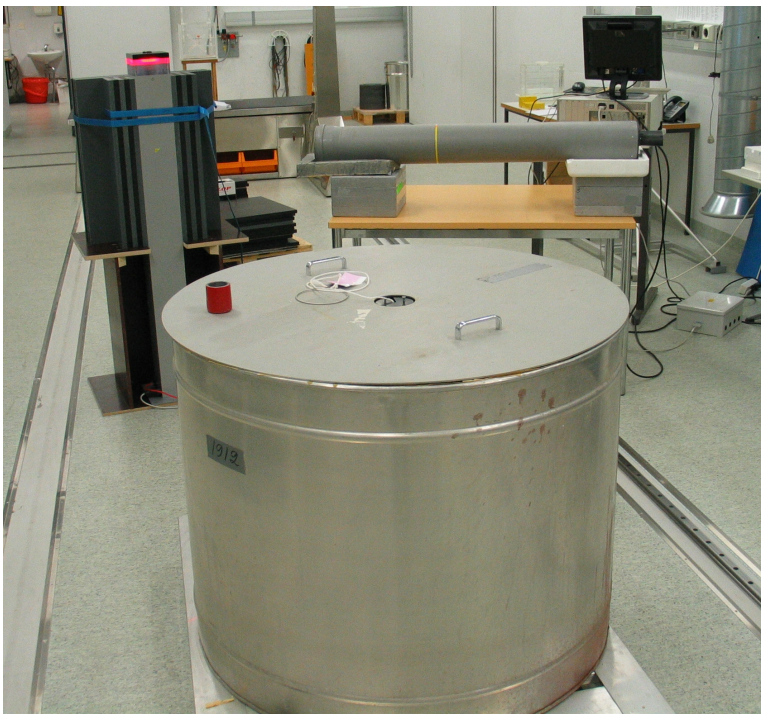

Figure 7.2: Thermo Fisher Scientific ^{3}He-based portal monitor on the right side and the NaI portal monitor boosted with 10 cm PVC/PE on the left side. SH2 (50 cm BPE) is at the front of the picture.

For the measurements, the He-based portal monitor was placed horizontally on styrene stands on a table. The distance between the centre of the tube and the floor was 1 m. Two measurement series were performed. First, the performance with different source shields was tested. These measurements were performed simultaneously with the He-based portal monitor and the NaI portal monitor at a source-detector distance of 2 m. Second, the distance dependence of the absolute efficiency up to a source-detector distance of 5 m was measured with both portal monitors. For all comparisons, the distance from the surfaces of the portal monitors to the centre of the source was equal. Figure 7.2 presents the portal monitors and SH2 (50 cm BPE).

Table 7.3: Absolute neutron detection efficiencies of the NaI and He portal monitors. The Norm. columns show absolute efficiencies normalized to the value for the respective source without neutron shielding (Cf2 or AmBe1/SH4)

Source	$\varepsilon_{abs,NaI}$	Norm.	$\varepsilon_{abs,He}$	Norm.
Cf2	$(3.6266\ 7)\times10^{-4}$	1	$(4.80\ 4)\times10^{-4}$	1
Cf2/SH5	$(3.41\ 2)\times10^{-5}$	0.094	$(1.88\ 2)\times10^{-5}$	0.039
Cf2/SH2	$(9.4\ 1)\times10^{-6}$	0.026	$(5.8\ 1)\times10^{-6}$	0.012
AmBe1/SH4	$(4.452\ 8)\times10^{-4}$	1	$(3.37\ 3)\times10^{-4}$	1
AmBe1/SH4/SH5	$(1.226\ 5)\times10^{-4}$	0.275	$(3.4\ 1)\times10^{-5}$	0.101
AmBe1/SH4/SH2	$(6.30\ 2)\times10^{-5}$	0.141	$(2.02\ 4)\times10^{-5}$	0.060

7.3.1 Efficiency comparison with different sources

Table 7.3 summarizes the absolute detection efficiencies of the portal monitors with the Cf1 and AmBe1 sources. With the bare Cf2 source, the absolute efficiency of the NaI portal monitor is about 76% of that of the He-based portal monitor. However, with the lead-shielded AmBe1 source, it is the He-based absolute efficiency that is 76% of that of the NaI portal monitor. The normalized columns show that the NaI portal monitor preserves its detection efficiency better than the He-based portal monitor when neutron shields are used. In fact, the NaI portal monitor has better performance than the He-based portal monitor in every case except with the bare Cf2 source.

This important result can be explained by two factors. First, the indirect detection method of the NaI portal monitor detects the gamma rays emitted directly by the source, since these are not effectively shielded by neutron shields. The neutron shields might also increase the rate of neutron capture reactions in the close environment of the source and the detector. This can further improve the detection efficiency of the NaI portal monitor. Second, the moderator of the He-based portal monitor might reduce the detection efficiency of shielded sources. This is because the shield moderates the neutrons, making neutron absorption in the He-tube moderator more probable. However, since the NaI portal monitor performs so much better in the AmBe1 case, the detection of the gamma rays seems to play a more important role than the absorption of neutrons in the He tube moderator.

The results are very interesting from security point of view. In an illicit trafficking scenario, one might expect that the neutron source is shielded to reduce the possibility of being detected. As the measurement results show, the NaI portal monitor is superior to the He-based portal monitor in these cases.

It should, however, be noted that the He-based portal monitor has a lower background count rate. In the radiation metrology laboratory, the background count rate was 0.5–0.8 cps. The signal-to-noise ratio is thus better for the He-based portal monitor in many cases (see Table 7.4). This does however not guarantee better limits of detection. Table 7.5 shows the MDAs in the different cases. The signal measurement time is t_S=1 s and background measurement time t_B=100 s. The false alarm rates are $\alpha = 10^{-6}$ and $\beta = 0.05$. For these values (see Appendix D), the detection limits are $L_D = 13.63$ cps (He, background 0.8 cps) and $L_D = 16.37$ cps (NaI, background 1.64 cps). The NaI portal monitor has lower (better) MDA values in every case except the bare Cf

Table 7.4: Signal-to-noise ratios of the portal monitors. The background count rates (noise) were measured in the radiation metrology laboratory.

Source	NaI S/N	He S/N
Cf2	579 ± 2	1600 ± 200
Cf2/SH5	54.5 ± 0.3	62 ± 8
Cf2/SH2	15.0 ± 0.2	19 ± 2
AmBe1/SH4	216.5 ± 0.8	349 ± 40
AmBe1/SH4/SH5	59.6 ± 0.3	34 ± 4
AmBe1/SH4/SH2	30.6 ± 0.2	20 ± 3

Table 7.5: Minimum detectable activities for $t_S = 1$ s and t_B =100 s

Source	MDA_{NaI} [Bq]	MDA_{He}[Bq]
Cf2	$(3.897\ 1)\times10^5$	$(2.45\ 2)\times10^5$
Cf2/SH5	$(4.14\ 6)\times10^6$	$(6.25\ 6)\times10^6$
Cf2/SH2	$(1.50\ 2)\times10^7$	$(2.04\ 4)\times10^7$
AmBe1/SH4	$(4.853\ 8)\times10^8$	$(5.34\ 4)\times10^8$
AmBe1/SH4/SH5	$(1.762\ 7)\times10^9$	$(5.3\ 2)\times10^9$
AmBe1/SH4/SH2	$(3.43\ 1)\times10^9$	$(8.9\ 2)\times10^9$

source case. In addition, the NaI portal monitor is probably more sensitive to the radiation leakage in the radiation metrology laboratory. Using background count rates measured outside the laboratory would thus probably favour the NaI portal monitor.

7.3.2 Source-detector distance dependence

The source-detector distance dependence was measured with the source Cf1 and is illustrated in Figure 7.3. The results are similar to those presented in section 6.4. The measurements show that the portal monitors have a very similar source-detector distance dependence (at least when the source-detector distance is $\geq$0.5 m). There are, however some differences. With one more data point (5 m) it was possible to fit the count rate data to the equation $ar^b + c$. For the He-based portal monitor, $b = -1.3$ and $c = 32$ cps. For the NaI portal monitor, the dependence is $b = -1.6$ and $c = 41$ cps. The large constant c comes from the baseline caused by the scattered neutrons in the laboratory. The higher value of c for the NaI portal monitor suggests that this detector is more sensitive to the scattered neutrons than the He-based portal monitor.

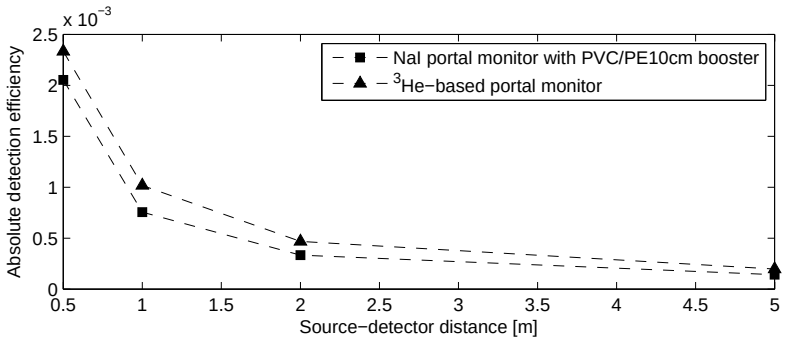

Figure 7.3: Absolute detection efficiencies of the bare Cf1 source with the portal monitors. The error margins (one standard deviation) are too small ($\leq$1%) to be shown in the figure.

Chapter 8

Conclusions

The results presented in this thesis demonstrate that a neutron detection ability can be added to a NaI detector with only slight modifications. One of the goals was to find an optimum converter, or „booster". For the used portal monitor, a 10-cm-thick booster consisting of PVC and PE is recommended as a good compromise between size, weight and performance. The better efficiency of PVC over steel is in line with the results presented in Ref. [3]. The neutron detection efficiency of the boosted portal monitor is comparable with that of a moderated ^{3}He tube of similar size. The NaI detector in fact has both superior detection efficiencies and MDA values in evasive scenarios and with AmBe sources, making it a very promising alternative for security applications.

Similar studies have been performed in e.g. Refs [3, 4], but these have been smaller studies compared to this thesis. The present measurements gave a good understanding of what the high-energy signal consists of. A large part of the signal is due to neutron capture reactions inside the detector, especially by ^{127}I. The booster improves the detection efficiency mostly by increasing the capture probability inside the detector, but also by capturing neutrons and emitting high-energy gamma rays. Due to the neutron capture reactions by ^{127}I, the converter has little effect without a thick enough booster. This suggests that only moderators should be used for small detectors, such as hand-held devices. Further insight into the underlying phenomena of the detection method could be gained by Monte Carlo simulations and comparisons between different types of detectors (e.g. $LaBr_3$ and NaI detectors of the same size).

The measurements indicate that the background radiation is not due to neutron capture reactions in the portal monitor, but mainly due to high-energy gamma rays from the environment. This could be confirmed by measurements with a controlled high-energy gamma ray and neutron background. No minimization of the background count rate was performed. A gamma shield could be used to lower the (low-energy) background count rate and thus improve gamma source MDAs in the direction of interest.

Appendix A

Gamma spectra with superimposed (n,γ) cross sections

This appendix contains measured gamma spectra with superimposed (n,γ) cross sections from Ref. [18]. The count rates of the spectra are on the left y-axes on logarithmic scales, while the cross sections are on the right y-axes on linear scales. The spectra have been divided into a low-energy and a high-energy part for better resolution. Only the cross sections of the most important isotopes are shown. Prompt and delayed gamma rays are discriminated with the labels p and d.

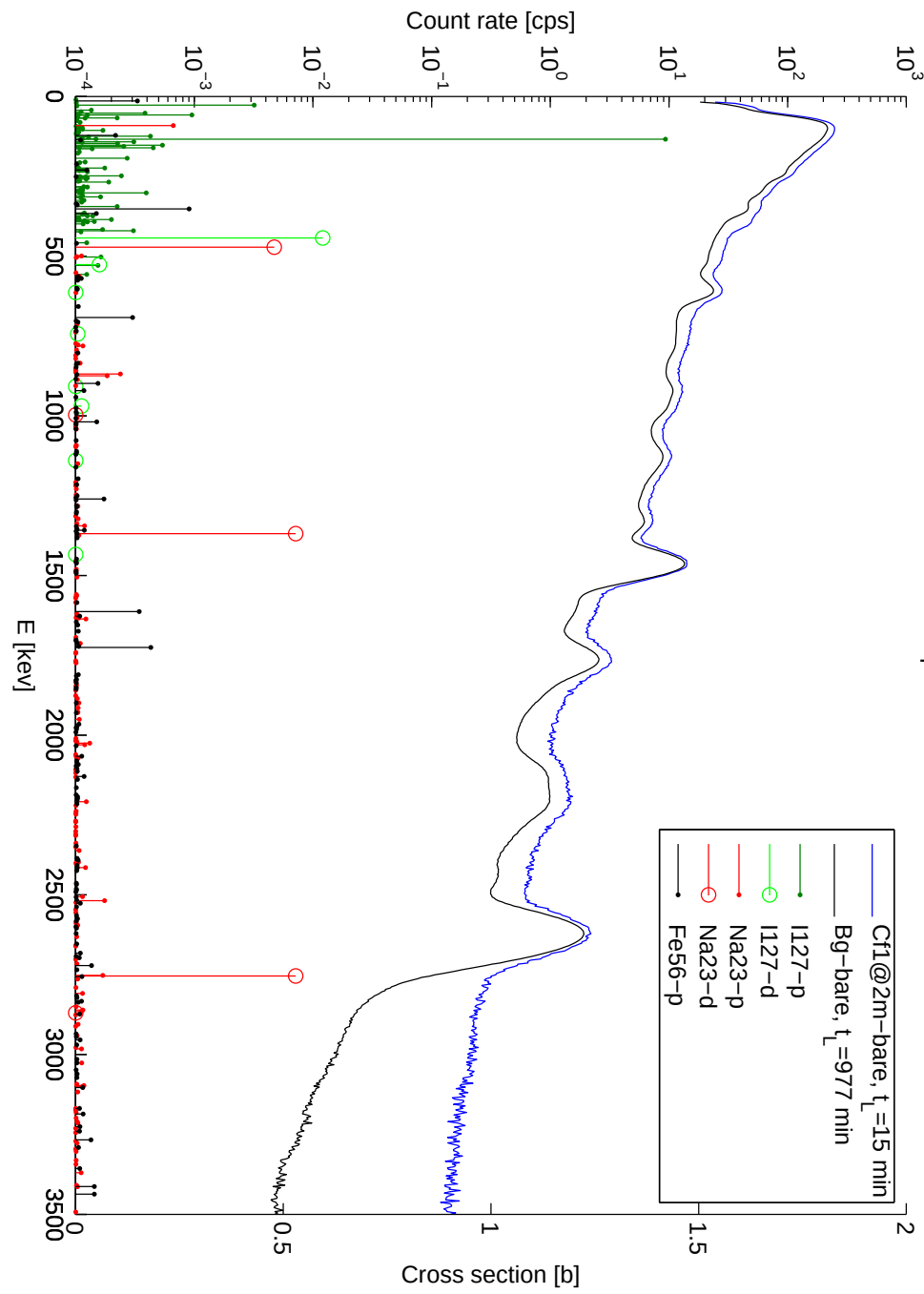

Figure A.0.1: Low-energy part of the Cf1 spectrum measured with the bare NaI portal monitor.

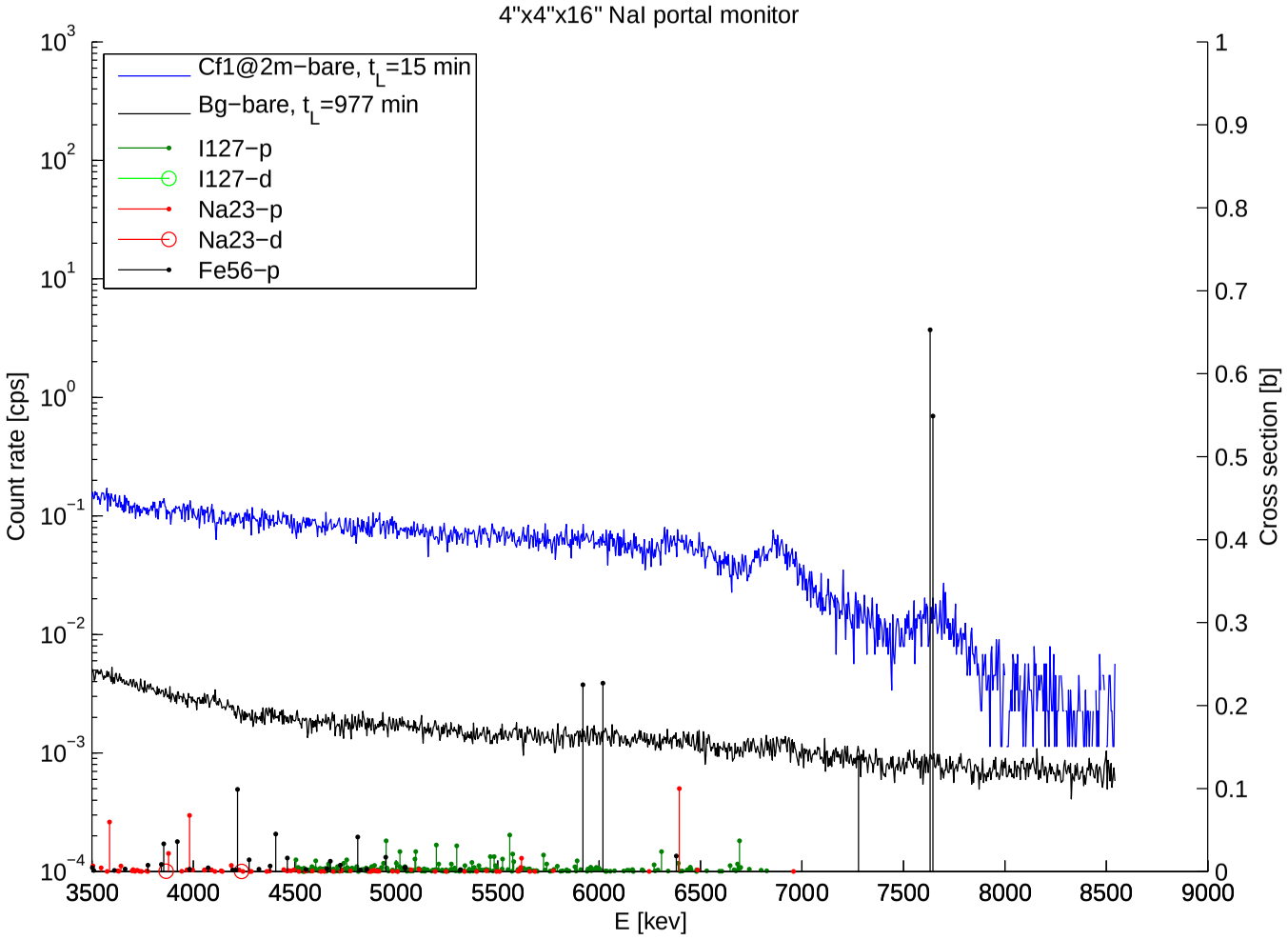

Figure A.0.2: High-energy part of the Cf1 spectrum measured with the bare NaI portal monitor.

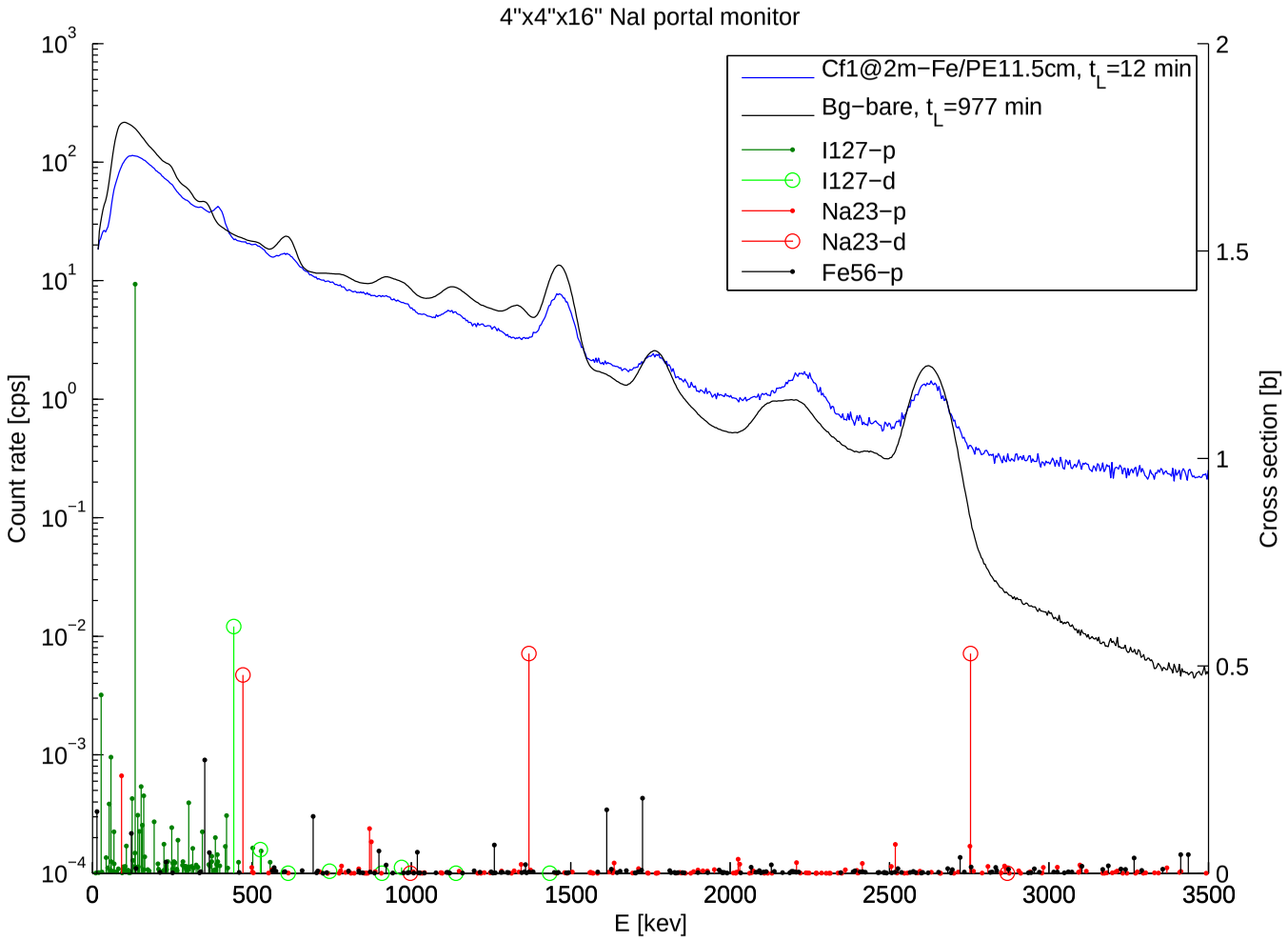

Figure A.0.3: Low-energy part of the Cf1 spectrum measured with the NaI portal monitor boosted with 11.5 cm of Fe/PE.

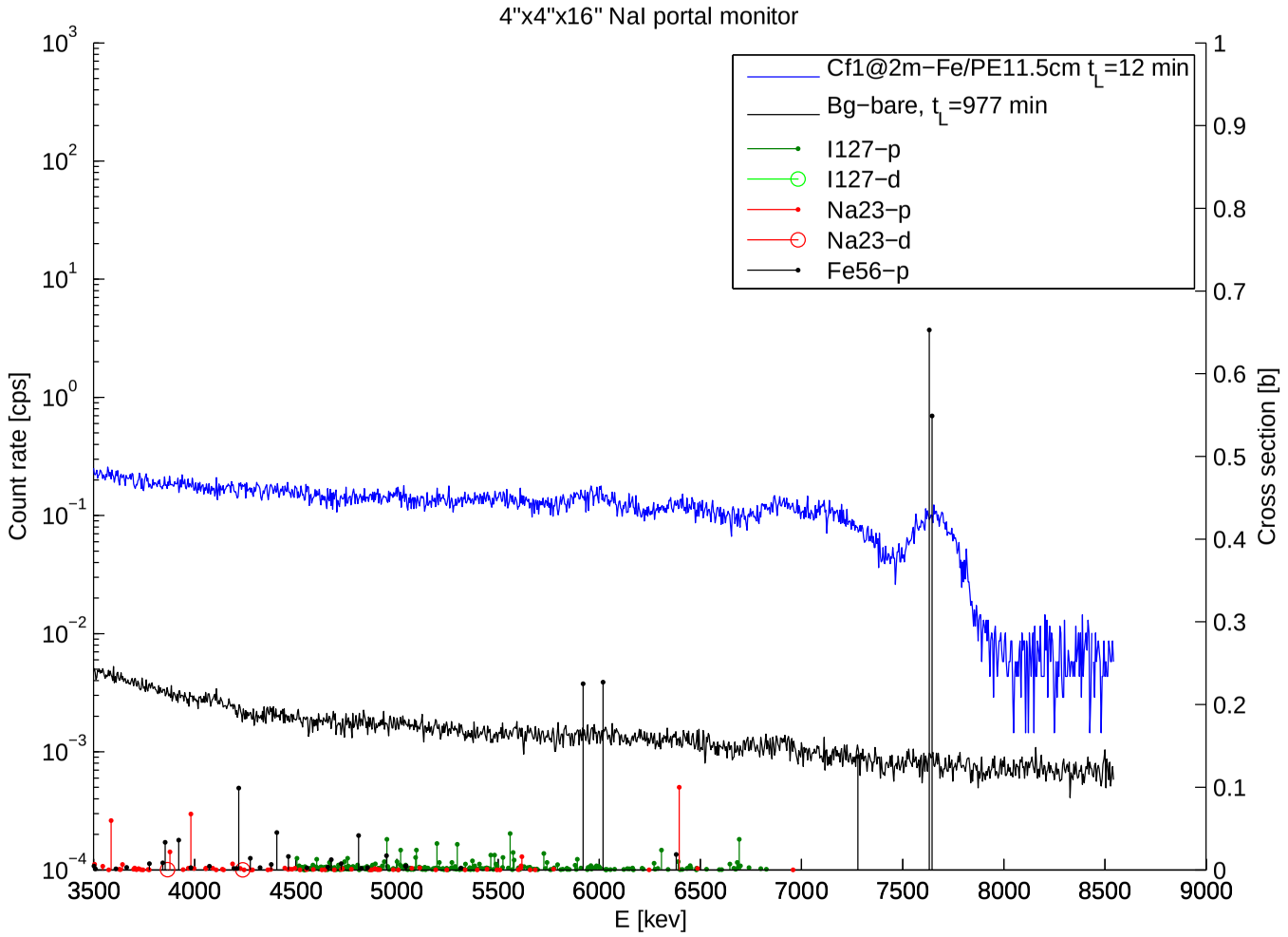

Figure A.0.4: High-energy part of the Cf1 spectrum measured with the NaI portal monitor boosted with 11.5 cm of Fe/PE

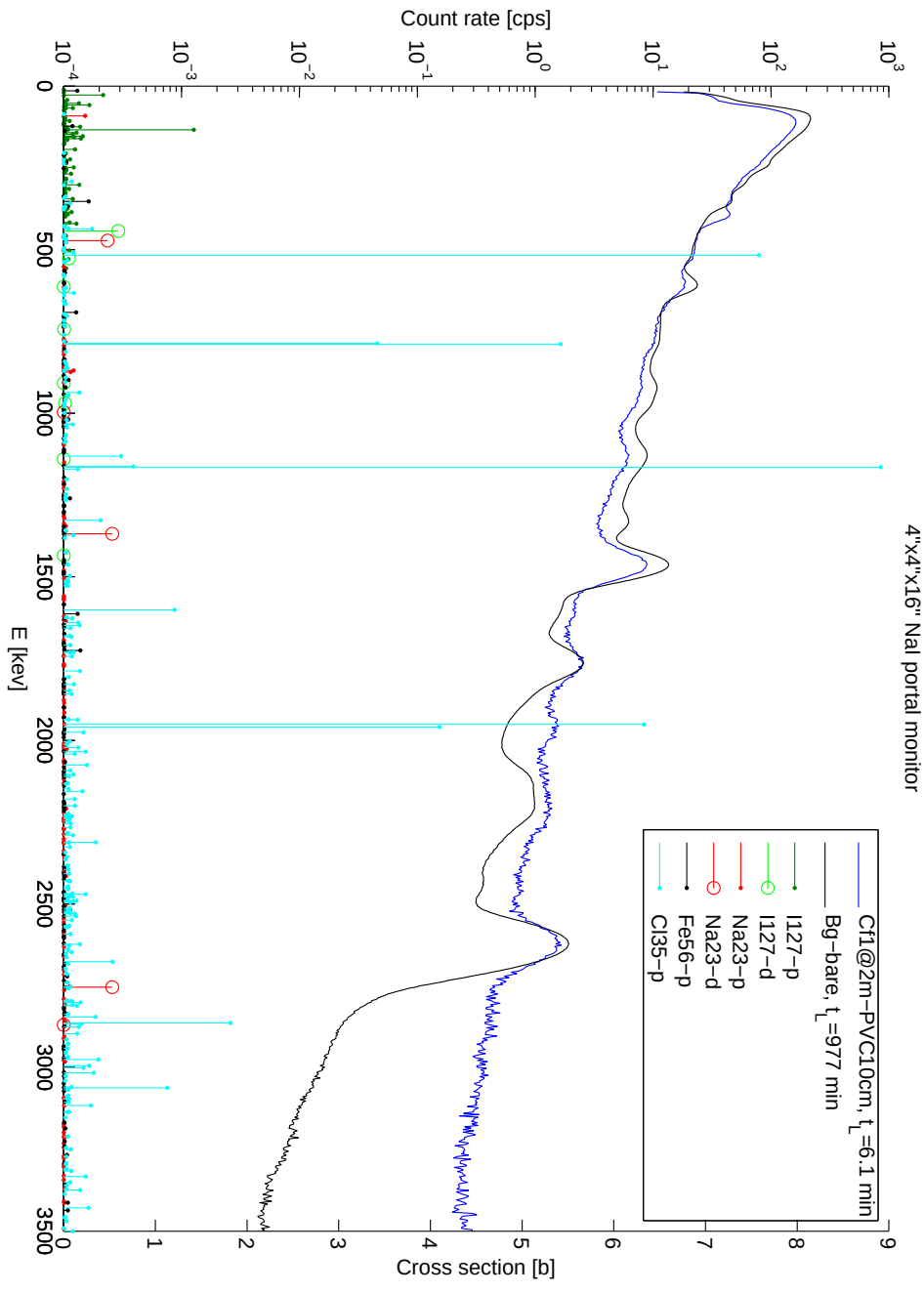

Figure A.0.5: Low-energy part of the Cf1 spectrum measured with the NaI portal monitor boosted with 10 cm of PVC

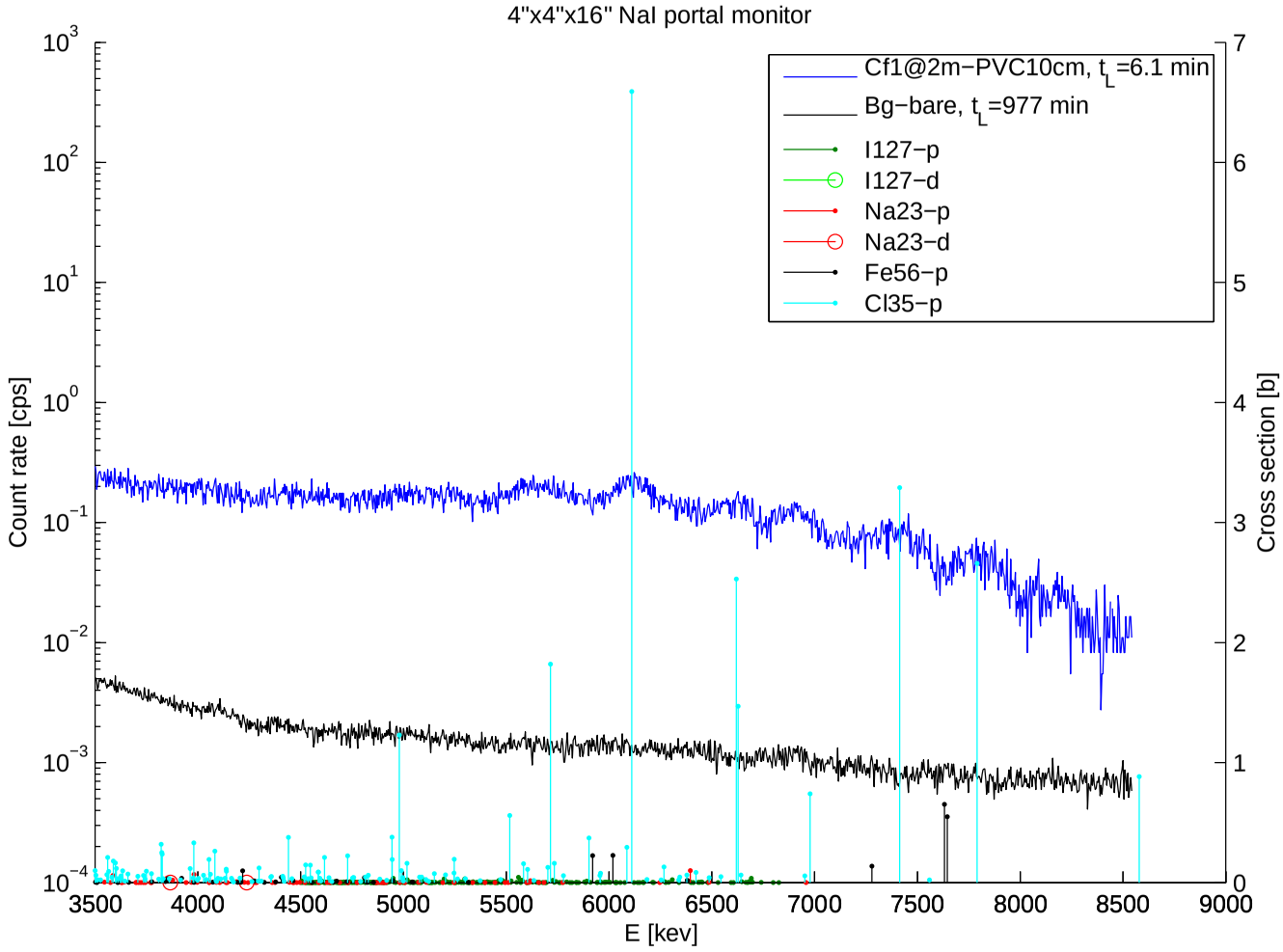

Figure A.0.6: High-energy part of the Cf1 spectrum measured with the NaI portal monitor boosted with 10 cm of PVC

Appendix B

Portable gamma spectrometers

B.1 5”x4” NaI detector

The cylindrical NaI detector had a 1024-channel MCA and covered the energy range 0–8.1 MeV. The low energy cut off was at channel 10 or 31.5642 keV. The spectra were recorded along with the sum from channels 437 to 1009 (3498.7 keV-8004.2 keV). The detector was operated along with the other portable detectors with a laptop running the Vasikka software.

Paraffin grains were used as a moderator. The detector was placed in a cylindrical plastic box, which was filled with paraffin grains. This surrounded the side of the detector with a 4.6-cm-thick paraffin layer. Due to the porosity of the moderator, the effective density of the paraffin was 0.43 g/cm3 (paraffin has a density of about 0.9 g/cm3).The paraffin also covered part of the back of the detector, but the front side was left uncovered. Figure B.1.1 shows the detector with its paraffin moderator. The bare detector is visible in Figure B.2.1.

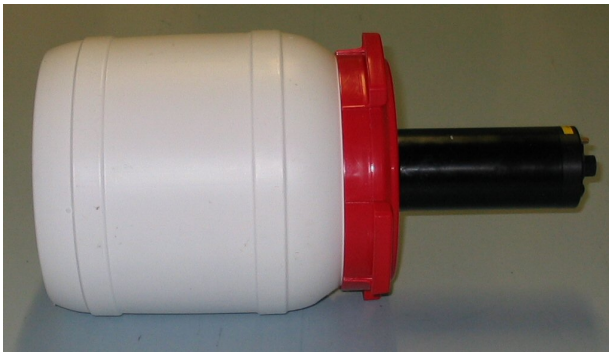

Figure B.1.1: 5”x4” NaI detector moderated with paraffin

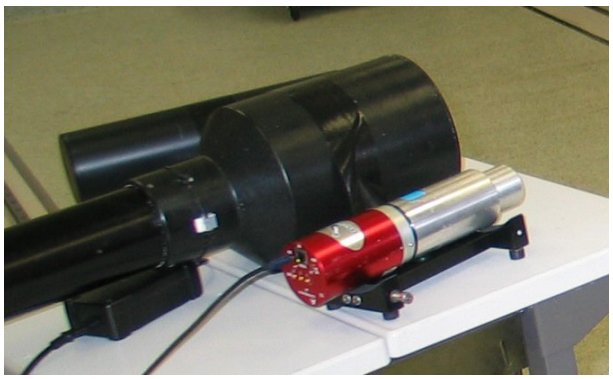

Figure B.2.1: 1.5”x1.5” $LaBr_3$ detector in front of the other portable detectors. The 5”x4” NaI detector is in the middle.

Figure B.3.1: BC-702 neutron detector in front of the 5”x4” NaI detector.

B.2 1.5”x1.5” $LaBr_3$ detector

The $LaBr_3$ detector was used with a 2048-channel MCA and was set to cover the energy range 0–5.1 MeV. The low-energy cut-off was at channel 7, referring to 21.0459 keV. The spectra were recorded along with the sum from channels 1415 to 2013 (3500.2 keV - 4999.0 keV). The $LaBr_3$ detector was moderated in the same way as the portable NaI detector, with a paraffin layer having a thickness of 6.1 cm. The bare detector is visible in front of the other portable detectors in Figure B.2.1.

B.3 BC-702 neutron detector

The BC-702 neutron detector was used as such and the neutron count rates were measured. The BC-702 detector uses a thin ZnS(Ag) scintillator loaded with ^{6}Li and has a very small gamma ray response. The detector is shown in Figure B.3.1.

Table B.4.1: Signal to noise ratios and neutron detection efficiencies of the bare and moderated (mod.) portable detectors. The values are calculated from measurements with the Cf1 source at a distance of 2 m from the detector surface. Values for the portal monitors are included for comparison. The source-detector distance of the ^{3}He tube was 2.05 m, since in this measurement the source was closer to the floor than the detector.

Detector	S/N	ϵ_{abs}	$\epsilon_{int,a}$ [%]	$\epsilon_{int,t}$[%]
5"x4" NaI	32	(4.10 1)$\times 10^{-5}$	16.27 5	9.19 3
5"x4" NaI, mod.	46	(6.20 3)$\times 10^{-5}$	24.6 1	5.65 2
1.5"x1.5" $LaBr_3$	17	(8.4 5)$\times 10^{-7}$	3.7 2	3.1 2
1.5"x1.5" $LaBr_3$, mod.	28	(1.40 3)$\times 10^{-6}$	6.2 1	0.338 8
BC702	44	(1.55 3)$\times 10^{-6}$	3.84 6	1.55 3
4"x4"x16" NaI (boosted)	92	(3.44 1)$\times 10^{-4}$	41.9 2	7.82 3
^{3}He tube	265	(4.85 5)$\times 10^{-4}$	65.8 6	20.2 2

B.4 Neutron detection efficiencies of the portable detectors

The neutron sensitivities and intrinsic efficiencies of the portable detectors are presented in Table B.4.1. The portal monitor results are also included for comparison[1]. Moderation increases ε_{abs} and $\varepsilon_{int,a}$, but the absolute efficiency does not increase enough to improve $\varepsilon_{int,t}$. The absolute efficiency of the moderated $LaBr_3$ detector is close to that of the BC702 detector. The total intrinsic efficiency of the bare $LaBr_3$ detector is better than that of the BC702 detector. Due to the higher background count rate of the $LaBr_3$ detector, the signal-to-noise ratio of the BC702 detector is better.

[1]The portable detector results are from the measurement campaigns in 2011, while the portal monitor results are from 2012.

Appendix C

Alternative booster structures

C.1 Moderator in front of the detector

Figure C.1.1 shows the absolute detection efficiency of the NaI portal monitor with large (54 cm x 65 cm) PE plates on the front side of the detector. With a thick layer of PE, the decrease in the absolute efficiency is much more dramatic than with the PE on the sides and back sides of the detector (see Figure 6.11). This is because the neutrons incident on the front side are absorbed by the hydrogen in PE. With even thicker layers of PE, the efficiency should saturate due to the unaffected scattered neutrons hitting the unmoderated sides of the detector.

The measurements were also performed with a PE6cm (the best booster containing only PE) and PVC/PE10cm booster. As shown in Figure C.1.2, 2 cm of PE in front of the detector increased the absolute efficiency slightly in the

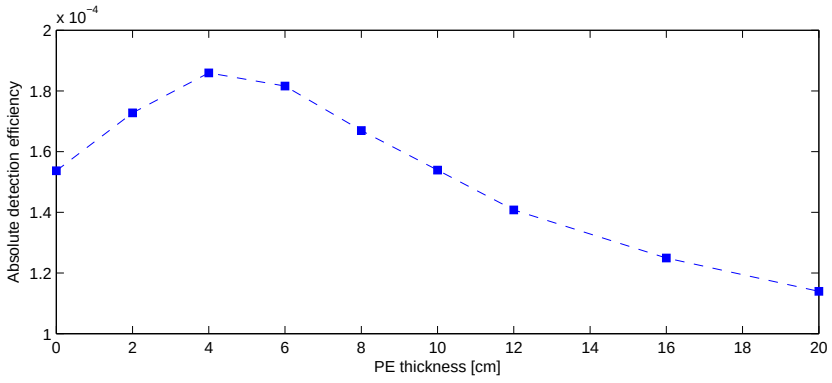

Figure C.1.1: Absolute neutron detection efficiency of the NaI portal monitor with different amounts of PE in front of the detector. The measurements were performed with the Cf1 source at a source-detector distance of 2 m. The error margins are too small to be shown in the figure (standard deviation $\leq$1%)

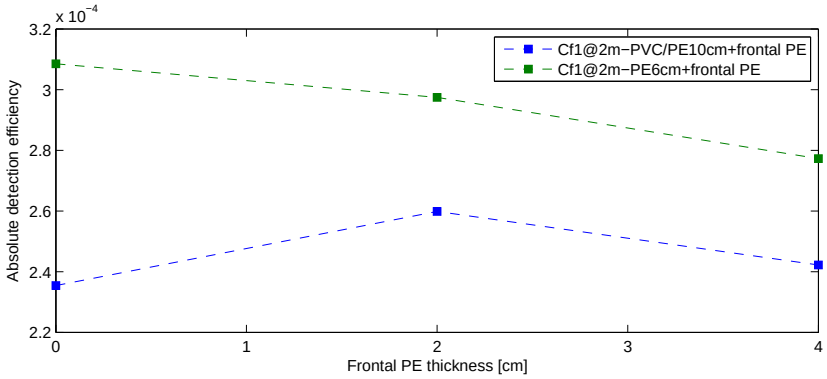

Figure C.1.2: Absolute neutron detection efficiency of the boosted NaI portal monitor with different amounts of PE in front of the detector. The error margins are too small to be shown in the figure (standard deviation $\leq 1\%$)

PE6cm case, but the frontal PE had only a negative effect in the PVC/PE10cm case. This difference could be due to the different thicknesses of the boosters. However, the difference might also be due to the different functions of the boosters. When only PE is used, the booster increases the efficiency only by increasing the quantity of moderated neutrons in the scintillator. Moderation by the frontal PE can thus improve the efficiency further, as long as the neutron absorption by the moderator does not grow too large. The PVC/PE booster increases the quantity of moderated neutrons in the scintillator, but also produces neutron-capture gamma rays. The frontal PE possibly shifts the neutron-capture gamma ray production closer to the surface of the booster and thus further away from the centre of the scintillator. This would reduce the detection efficiency of these gamma rays.

C.2 Booster structure

Several booster configurations were tested. The sandwich structure with alternating layers of converter and moderator material (starting and ending with the converter material) was found to be the best solution. The only improvement was obtained when steel converters were used and the amount of steel was decreased. The improvement was not large, and even this improvement is not certain, because of a possible error in the measurements[1]. Tables C.2.1, C.2.2 and C.2.3 show normalized absolute efficiencies with different booster structures.

[1] The efficiency of the Fe/PE sandwich booster was for some reason smaller in this series of measurements compared to previous measurements.

Table C.2.1: The absolute efficiency of 6–7.2-cm-thick boosters normalized to the absolute efficiency with the 6-cm-thick PE booster. The measurements were performed with the Cf1 source at a source-detector distance of 2 m. The booster structure (plate order starting from the detector side) is shown in the left column. The standard deviation is ≤1%

Booster structure	Norm. ε_{abs} [%]
PE/PE/PE	100
PVC/PE/PVC	119
PVC/PVC/PVC	112
PE/PE/PE/Fe/Fe/Fe/Fe	108
Fe/PE/Fe/PE/Fe/PE/Fe	107
Fe/PVC/Fe/PVC/Fe/PVC/Fe	101
Fe/Fe/PE/PE/PE/Fe/Fe	96.4
Fe/Fe/Fe/Fe/PE/PE/PE	85.2

Table C.2.2: The absolute efficiency of 10-cm-thick PVC boosters normalized to the absolute efficiency with the PVC/PE10cm sandwich. The measurements were performed with the Cf1 source at a source-detector distance of 2 m. The booster structure (plate order starting from the detector side) is shown in the left column. The standard deviation is ≤1%

Booster structure	Norm. ε_{abs} [%]
PVC/PE/PVC/PE/PVC	100
PE/PE/PVC/PVC/PE	99.9
PE/PE/PE/PVC/PVC	96.1
PE/PE/PVC/PE/PE	95.0
PE/PE/PE/PE/PE	82.7

Table C.2.3: The absolute efficiency of approximately 10-cm-thick Fe boosters normalized to the absolute efficiency with the PVC/PE10cm sandwich. The measurements were performed with the Cf1 source at a source-detector distance of 2 m. The booster structure (plate order starting from the detector side) is shown in the left column. The standard deviation is ≤1%

Booster structure	Norm. ε_{abs} [%]
PVC/PE/PVC/PE/PVC	100
PE/Fe/PE/Fe/PE/Fe/PE/Fe/PE	88.3
PE/PE/Fe/PE/Fe/PE/Fe/PE/Fe	87.4
PE/PE/Fe/PE/PE/Fe/PE/Fe	84.6
Fe/PE/Fe/PE/Fe/PE/Fe/PE/Fe/PE	83.3
PE/PE/PE/PE/PE	82.7
PE/PE/Fe/PE/PE/PE/Fe	81.5

Appendix D

Limits of detection using Poisson statistics

D.1 Poisson distribution

For events occurring independently and with a fixed average rate, the probability that exactly k events have occurred during a time interval t is given by the Poisson distribution

$$f(k, \mu) = \frac{\mu^k e^{-\mu}}{k!} \tag{D.1.1}$$

where μ is the average number of events in the time interval t. If the number of counts is large enough, the normal distribution can be used as an approximation for the Poisson distribution. This is often the case in radioactivity measurements. However, the Poisson distribution has to be used in some special cases. One of these is the detection of neutron sources with high-energy gamma rays, since the measurement times can be short (1 s) and the count rate is low.

D.2 Currie limits of detection

For radioactivity measurements, Currie [26] defines a critical level L_C and a detection limit L_D. L_C is calculated from the background count rate of the detection system and depends on the chosen false positive alarm probability α. L_D is the net signal value representing the minimum detectable activity and depends on L_C and the false negative alarm probability β. The limits are defined by the constraints (see e.g. Ref. [27])

$$P(b > L_C | \mu_S = 0) \leq \alpha \tag{D.2.1}$$

$$P(S < L_C | \mu_S = L_D) \leq \beta \tag{D.2.2}$$

where b is the measured background signal. S is the number of counts caused by a source inducing on average μ_S counts.

D.3 Poisson-normal approximation

For a sufficiently large average count rate, the number of counts can be assumed to follow a normal distribution with a variance $\sigma^2 = \mu$. The limits of detection L_C and L_D are then given by [26]

$$L_C = k_{1-\alpha}\sqrt{\mu_B\left(1+\frac{1}{r}\right)} = k_{1-\alpha}\sqrt{\mu_B \eta} \tag{D.3.1}$$

$$L_D = L_C + \frac{k_{1-\beta}^2}{2}\left\{1+\left[1+\frac{4L_C}{k_{1-\beta}^2}+\frac{4L_C^2}{k_{1-\alpha}^2 k_{1-\beta}^2}\right]^{1/2}\right\} \tag{D.3.2}$$

where μ_B is the mean of the background signal, r is the ratio of the background measurement time t_B and the signal measurement time t_S and $\eta = 1+1/r$. $k_{1-\alpha}$ and $k_{1-\beta}$ are the multiplicative factors of the standard deviations corresponding to the probabilities 1-α and 1-β.

Perhaps the most important restriction of the Poisson-normal approximation is due to the skewness of the Poisson distribution. For sufficiently low backgrounds, the Poisson-normal approximation cannot be used. For a background count rate of 1 cps, the Poisson-normal approximation would give $L_C = 4.8$ cps and $L_D = 10.3$ cps for $\alpha = 10^{-6}$, $\beta = 0.05$ and $r = 100$. As will be shown in the following sections, the correct solution is $L_C = 8$ cps and $L_D = 14.7$ cps.

D.4 Exact Poisson solutions

For well-known backgrounds, the criteria of equation (D.2.1) and (D.2.2) can be used to tabulate or plot the limits of detection for given parameters. Such tables are presented at the end of this appendix. If the background is measured and not assumed to be sufficiently well-known, the problem is to detect a statistically significant difference between two measured signals.

The problem can be solved by calculating the joint probability of detecting the measured number of background counts b in the background measurement time t_B and detecting k counts in the signal measurement time t_S. Since the average μ_B of the background distribution is unknown, we integrate over all possible values. The cumulative probability up to the gross critical limit Y_C should be equal to or larger than 1-α. This gives the following criteria (suggested by S. Ihantola, STUK):

$$\sum_{k=0}^{Y_C}\int_0^\infty f(b,\mu_B) f(k,\frac{\mu_B}{r}) d\mu_B \geq 1-\alpha \tag{D.4.1}$$

where $r = t_B/t_S$. The integral can be solved using the definition of the Gamma function. The criterion can thus be rewritten as

$$\sum_{k=0}^{Y_C}\frac{\left(1+\frac{1}{r}\right)^{-b-k-1}\Gamma(b+k+1)}{b!k!} \geq 1-\alpha \tag{D.4.2}$$

This criterion is the same as that cited in [28]

$$\sum_{k=0}^{Y_C}\binom{b+k}{b}\left(\frac{t_S}{t_S+t_B}\right)^k\left(\frac{t_B}{t_S+t_B}\right)^{b+1} \geq 1-\alpha \tag{D.4.3}$$

The net detection limit L_D is defined by the criterion [28]

$$\sum_{n=0}^{\infty}\left(\frac{b^n e^{-b}}{n!}\sum_{k=0}^{Y_C(n)}\frac{\left(\frac{b}{r}+L_D\right)^k e^{-(\frac{b}{r}+L_D)}}{k!}\right)=\beta \tag{D.4.4}$$

The critical limit Y_C should thus be calculated for each background value n. In practice, the first sum is limited to a value of n for which the Poisson probability is sufficiently small.

The limits of detection calculated in this thesis are slightly higher than those tabulated in Ref. [28], although the same equations have been used. However, L. A. Currie presents a similar approach for calculating limits of detection in Ref. [29]. Currie presents limits of detection for paired observations ($t_B = t_S$ and $\alpha = \beta = 0.05$) that are in line with the results presented in this appendix. It is possible that the infinite sum in equation (D.4.4) was cut off too early in Ref. [28].

D.5 Numerical solution using MATLAB

D.5.1 Well-known background

With a well-known background, it is straightforward to apply criteria ((D.2.1)) and ((D.2.2)). With future real-time implementations in Vasikka in mind, the MATLAB script was written using a Poisson look-up table (see table D.5.1). Two simple algorithms were written. The first algorithm searches for the right column for a given μ to find Y_C. The second algorithm searches for the cell with the cumulative probability closest to (but smaller than) β given Y_C (represented by a column in the table). Y_D is then simply the average μ represented on the row of the cell.

D.5.2 Paired observations

Equations (D.4.2) and (D.4.4) were solved numerically using MATLAB. The limits of detection were calculated for background count values from 0 to $10t_B$. Binary search algorithms were used to iteratively find the solutions to the criteria. The algorithm searching for Y_D was stopped when the error margin was $\leq$0.1%.

Table D.5.1: Look-up table with cumulative Poisson probabilities for different averages.

μ	$\sum_{k=0}^{0} f(k,\mu)$	$\sum_{k=0}^{1} f(k,\mu)$	$\sum_{k=0}^{2} f(k,\mu)$	...	$\sum_{k=0}^{300} f(k,\mu)$
0	1	1	1	...	1
0.001	0.9990	1.000	1.000	...	1.000
0.002	0.9980	1.000	1.000	...	1.000
...					
59.999	8.8×10^{-27}	5.3×10^{-25}	1.6×10^{-23}	...	1.000

Because of the large numbers involved, the criteria were rewritten in logarithmic form (utilizing $x! = \Gamma(x+1)$ and the `gammaln(x)`=$ln(\Gamma(x))$ MATLAB function). The infinite sum in criterion (D.4.4) was cut off at n = 20+20t_B.

D.6 Gross limits of detection for well-known backgrounds

Table D.6.1: Gross detection limits for well-known backgrounds. False alarm rates are $\alpha \leq 0.05$ and $\beta = 0.05$. The actual α grows monotonically, with the lowest value shown in the first column.

α (minimum)	μ_B (range)	Y_C ($\alpha \leq 0.05$)	$Y_D(\beta = 0.05)$
-	0.00-0.051	0	3.00
0.0013	0.052-0.36	1	4.74
0.0058	0.36-0.82	2	6.30
0.0098	0.82-1.37	3	7.75
0.013	1.37-1.97	4	9.15
0.016	1.97-2.61	5	10.51
0.018	2.61-3.29	6	11.84
0.019	3.29-3.98	7	13.15
0.021	3.98-4.70	8	14.43
0.022	4.70-5.42	9	15.71
0.023	5.42-6.17	10	16.96

Table D.6.2: Gross detection limits for well-known backgrounds. False alarm rates are $\alpha \leq 10^{-6}$ and $\beta = 0.05$. The actual α grows monotonically, with the lowest value shown in the first column.

α (minimum)	μ_B (range)	Y_C ($\alpha \leq 10^{-6}$)	Y_D (β=0.05)
0	0	0	3
5.0×10^{-7}	0.001	1	4.74
1.3×10^{-9}	0.002-0.02	2	6.30
6.6×10^{-9}	0.02-0.07	3	7.75
1.4×10^{-8}	0.07-0.17	4	9.15
2.9×10^{-8}	0.17-0.31	5	10.51
4.5×10^{-8}	0.31-0.50	6	11.84
6.2×10^{-8}	0.50-0.73	7	13.15
8.1×10^{-8}	0.73-0.99	8	14.43
9.8×10^{-8}	0.99-1.28	9	15.71
1.2×10^{-7}	1.28-1.60	10	16.96
1.3×10^{-7}	1.60-1.94	11	18.21
1.5×10^{-7}	1.94-2.31	12	19.44
1.6×10^{-7}	2.31-2.69	13	20.67
1.8×10^{-7}	2.70-3.10	14	21.89
1.9×10^{-7}	3.10-3.52	15	23.10
2.0×10^{-7}	3.52-3.96	16	24.30
2.2×10^{-7}	3.96-4.42	17	25.50
2.3×10^{-7}	4.42-4.88	18	26.69
2.4×10^{-7}	4.88-5.36	19	27.88
2.5×10^{-7}	5.36-5.86	20	29.06
2.6×10^{-7}	5.86-6.36	21	30.24

D.7 Gross limits of detection for paired measurements with $\alpha \leq 0.05$ and $\beta = 0.05$

Table D.7.1: Gross detection limits for paired measurements with $t_B = t_S = 1$. False alarm rates are $\alpha \leq 0.05$ and $\beta = 0.05$. The actual α is shown in the first column.

α'	b	Y_C ($\alpha \leq$0.05)	Y_D (β=0.05)
0.031	0	4	9.15
0.035	1	6	12.85
0.033	2	8	15.45
0.046	3	9	17.79
0.038	4	11	20.01
0.048	5	12	22.09
0.039	6	14	24.05
0.047	7	15	25.93
0.038	8	17	27.75
0.044	9	18	29.54
0.049	10	19	31.30

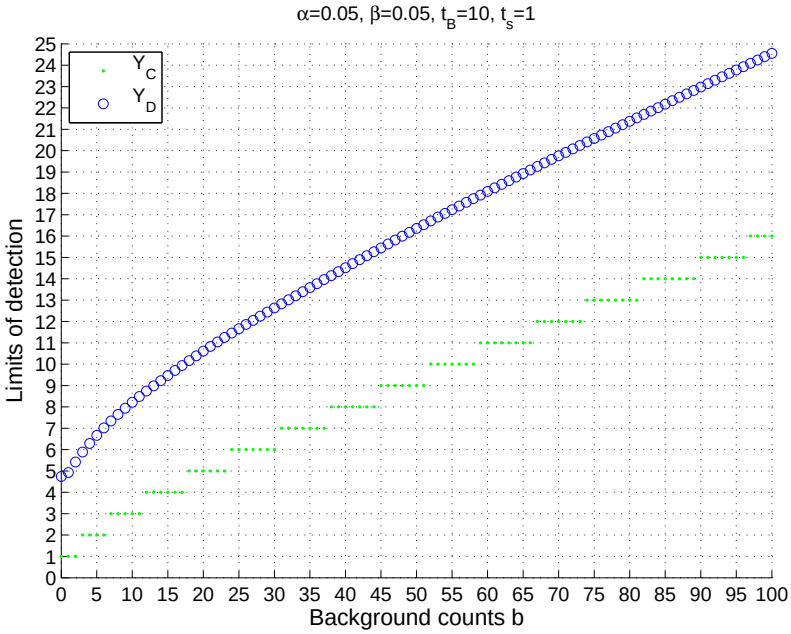

Figure D.7.1: Gross detection limits for paired measurements with $t_B = 10$ and $t_S = 1$. False alarm rates are $\alpha \leq 0.05$ and $\beta = 0.05$.

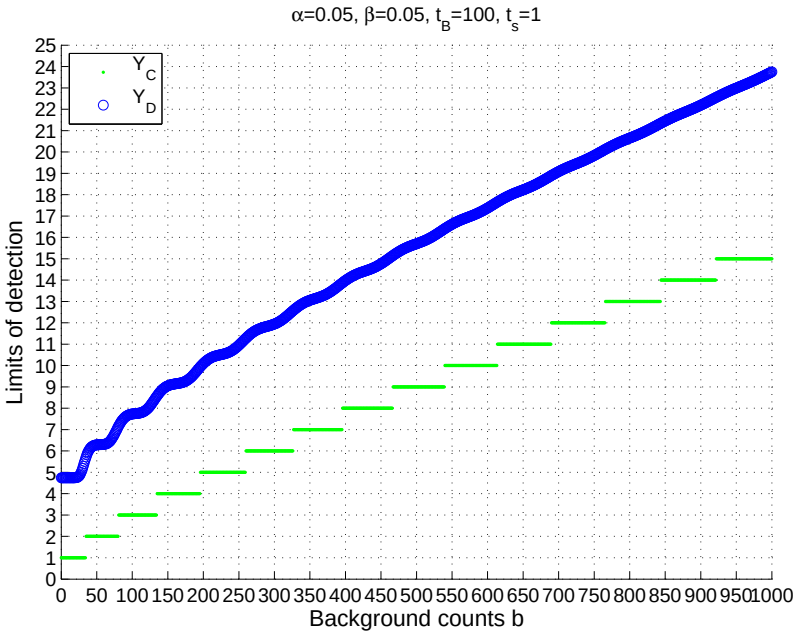

Figure D.7.2: Gross detection limits for paired measurements with $t_B = 100$ and $t_S = 1$. False alarm rates are $\alpha \leq 0.05$ and $\beta = 0.05$.

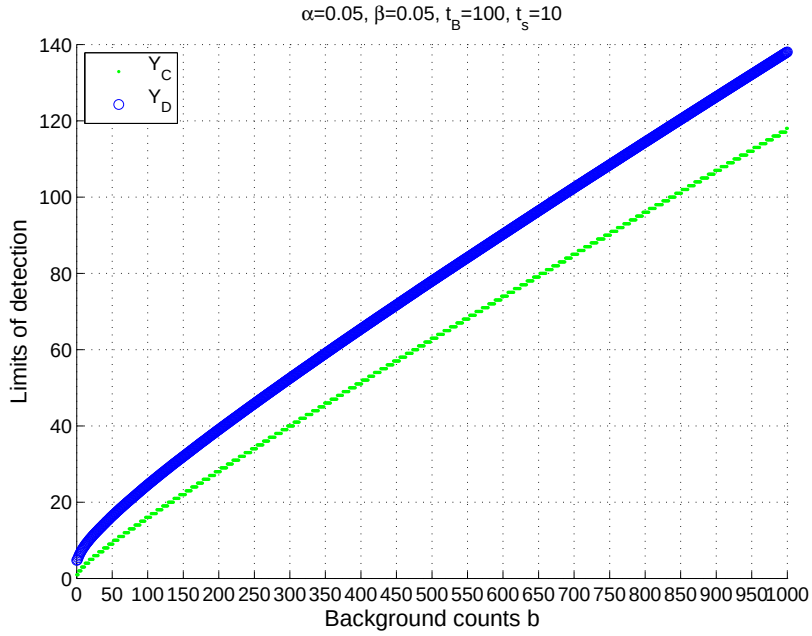

Figure D.7.3: Gross detection limits for paired measurements with $t_B = 100$ and $t_S = 10$. False alarm rates are $\alpha \leq 0.05$ and $\beta = 0.05$.

D.8 Gross limits of detection for paired measurements with $\alpha \leq 10^{-6}$ and $\beta = 0.05$

Table D.8.1: Gross detection limits for paired measurements with $t_B = t_S = 1$. False alarm rates are $\alpha \leq 10^{-6}$ and $\beta = 0.05$. The actual α is shown in the first column.

α'	b	Y_C ($\alpha \leq 10^{-6}$)	Y_D (β=0.05)
9.5×10^{-7}	0	19	27.88
7.7×10^{-7}	1	23	34.08
8.1×10^{-7}	2	26	38.33
7.0×10^{-7}	3	29	41.92
9.7×10^{-7}	4	31	45.16
6.9×10^{-7}	5	34	48.22
8.2×10^{-7}	6	36	51.14
9.2×10^{-7}	7	38	53.88
9.8×10^{-7}	8	40	56.44
6.1×10^{-7}	9	43	58.87
6.2×10^{-7}	10	45	61.23

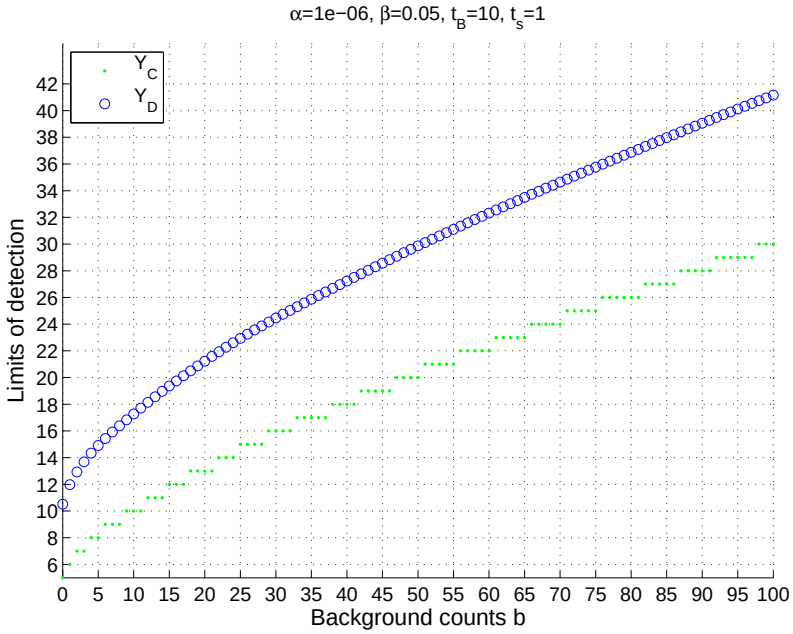

Figure D.8.1: Gross detection limits for paired measurements with $t_B = 10$ and $t_S = 1$. False alarm rates are $\alpha \leq 10^{-6}$ and $\beta = 0.05$.

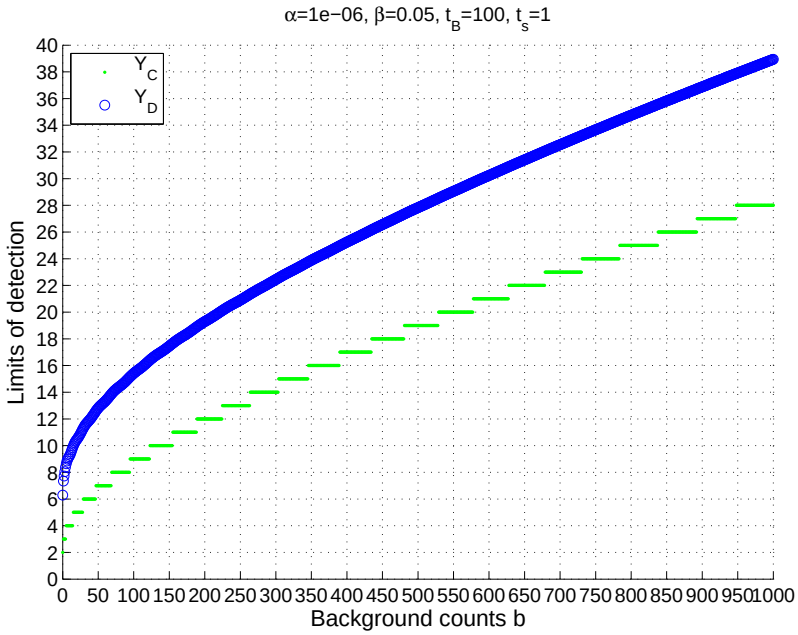

Figure D.8.2: Gross detection limits for paired measurements with $t_B = 100$ and $t_S = 1$. False alarm rates are $\alpha \leq 10^{-6}$ and $\beta = 0.05$.

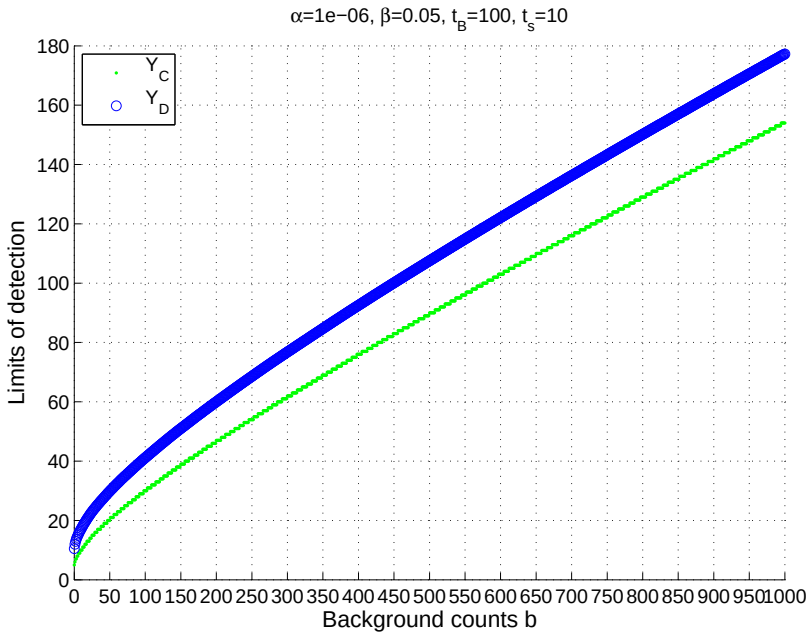

Figure D.8.3: Gross detection limits for paired measurements with $t_B = 100$ and $t_S = 10$. False alarm rates are $\alpha \leq 10^{-6}$ and $\beta = 0.05$.

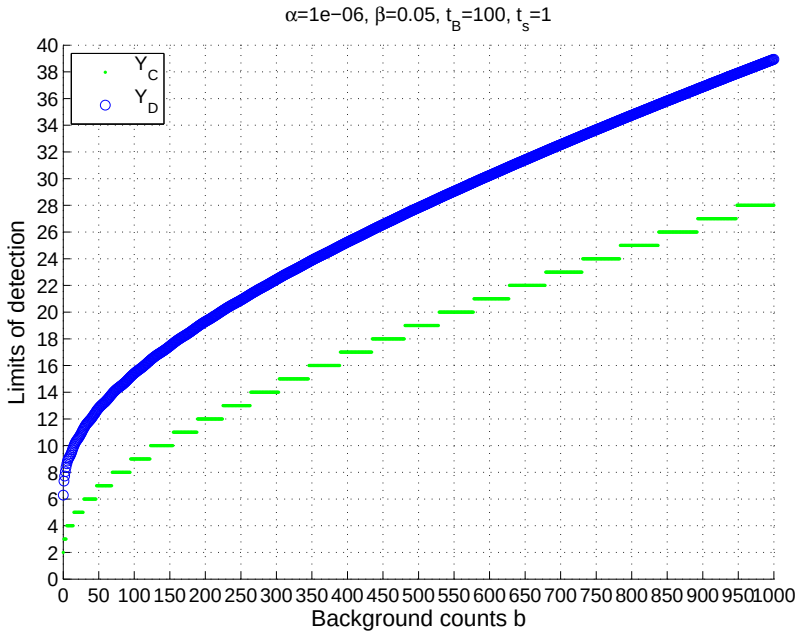

Figure D.8.4: Gross detection limits for paired measurements with $t_B = 100$ and $t_S = 1$. False alarm rates are $\alpha \leq 10^{-6}$ and $\beta = 0.05$.

Bibliography

[1] H. Toivonen. Characterization of an ^{241}Am/Be source. Technical Report TTL-TECDOC-2008-009, STUK, 2008. Internal research report.

[2] K. Peräjärvi, A. Hakanen, T. Siiskonen, T. Karhunen, A.-P. Sihvonen, P. Smolander, J. Turunen, S. Ihantola, and H. Toivonen. Neutroni-ilmaisintestit. Technical Report TTL-TECDOC-2011-2, STUK, 2011. Internal research report.

[3] D. J. Mitchell, L. T. Harding, and K. R. Smith. Neutron detection with gamma-ray spectrometers for border security applications. *IEEE Transactions on nuclear science*, 57(4), 2010.

[4] D. J. Mitchell and C. Brusseau. Neutron counting and gamma spectroscopy with PVT detectors. Technical Report SAND2011-4361, Sandia National Laboratories, 2011.

[5] J. E. Stewart. Principles of total neutron counting. In D. Reilly, N. Ensslin, and H. Smith, Jr., editors, *Passive Nondestructive Assay of Nuclear Materials*. 1991.

[6] Evaluated nuclear data file ENDF/B-VII.0. Retrieved from the National Nuclear Data Center, http://www.nndc.bnl.gov . Accessed Oct. 2011 – Jan. 2012.

[7] Jeff-3.1 library. Retrieved from the National Nuclear Data Center, http://www.nndc.bnl.gov . Accessed Oct. 2011 – Jan. 2012.

[8] Glenn F. Knoll. *Radiation Detection and Measurement 4th ed.* John Wiley & Sons, Inc., 2010.

[9] N. Ensslin. The origin of neutron radiation. In D. Reilly, N. Ensslin, and H. Smith, Jr., editors, *Passive Nondestructive Assay of Nuclear Materials*. 1991.

[10] T. E. Valentine. Evaluation of prompt fission gamma rays for use in simulating nuclear safeguard measurements. *Annals of Nuclear Energy*, 28:191, 2001.

[11] A.B. Smith, P. R. Fields, and A. M. Friedman. Prompt gamma rays accompanying the spontaneous fission of Cf^{252}. *Physical review*, 104(3):699, 1956.

[12] T. E. Valentine. MCNP-DSP users manual. Technical Report ORNL/TM-13334, R2, Oak Ridge National Laboratory, 2001.

[13] R. J. et al Gehrke. The γ-ray spectrum of ^{252}Cf and the information contained within it. *Nuclear Instruments and Methods in Physics Research B*, 213, 2004.

[14] J. W. Marsch, D. J. Thomas, and M. Burke. High resolution measurements of neutron energy spectra from Am-Be and Am-B neutron sources. *Nuclear Instruments and Methods in Physics Research A*, 366:340, 1955.

[15] H. R. Vega-Carrillo, E. Manzanares-Acuña, A. M. Becerra-Ferreiro, and A. Carrillo-Nuñez. Neutron and gamma-ray spectra of ^{239}PuBe and ^{241}AmBe. *Applied Radiation and Isotopes*, 57:167, 2002.

[16] P. Rinard. Neutron interactions with matter. In D. Reilly, N. Ensslin, and H. Smith, Jr., editors, *Passive Nondestructive Assay of Nuclear Materials*. 1991.

[17] Evaluated nuclear data file ENDF/B-VII.0. Plotted using http://www.nndc.bnl.gov/sigma/ on Dec. 22. 2011.

[18] IAEA. Database for prompt gamma-ray neutron activation analysis. http://www-nds.iaea.org/pgaa . Accessed in 2011.

[19] Nucleonica. http://nucleonica.com . Accessed in 2011.

[20] R. P. et al Gardner. NaI detector neutron activation spectra for PGNAA applications. *Applied Radiation and Isotopes*, 53, 2000.

[21] S. Croft and J. Chapman. The use of ^{252}Cf for calibrating safeguards monitors. Technical report, Canberra Industries, Inc., 2005.

[22] R. T. Kouzes. Passive neutron detection for interdiction of nuclear materials at borders. *Nuclear Instruments and Methods in Physics Research A*, 584, 2008.

[23] K. O'Brien. Cosmic ray induced neutron background source and fluxes for geometries of air over water, ground, iron and aluminium. *Journal of geophysical research*, 83, 1978.

[24] R. J. Sheu. A study of the cosmic-ray neutron field near interfaces. *Nuclear instruments and methods in physics research A*, 476, 2002.

[25] J. H. Hubbell and S. M. Seltzer. Tables of x-ray mass attenuation coefficients and mass energy-absorption coefficients from 1 kev to 20 MeV for elements Z = 1 to 92 and 48 additional substances of dosimetric interest. http://www.nist.gov/pml/data/xraycoef/index.cfm . Last update 2004. Accessed on Jan. 10 2012.

[26] L. Currie. Limits for qualititative detection and quantitative determination. *Analytical chemistry*, 40, 1968.

[27] L. Currie. The measurement of environmental levels of rare gas nuclides and the treatment of very low-level data. *IEEE Transactions on Nuclear Science*, 19, 1972.

[28] J. Griggs (editor). Multi-agency radiological laboratory analytical protocol manual. Technical Report NUREG-1576, 2004.

[29] L. A. Currie. On the detection of rare, and moderately rare, nuclear events. *Journal of Radioanalytical and Nuclear Chemistry*, 276(2), 2008.